이학박사 학위논문

Enhancement of 3-dimensional positioning accuracy in PET detector for high resolution PET system

고해상도 PET 시스템을 위한 PET 검출기의 3차원 위치 정보 정확도 향상 기술 개발

2018 년 2월

서울대학교 대학원
의학과 협동과정 방사선응용생명과학 전공

이 민 선

Ph.D. Dissertation of
Degree of Doctor of Philosophy in Science

Enhancement of 3-dimensional positioning accuracy in PET detector for high resolution PET system

고해상도 PET 시스템을 위한 PET 검출기의 3차원 위치 정보 정확도 향상 기술 개발

February 2018

Graduate School of College of Medicine
Seoul National University
Interdisciplinary Program in Radiation Applied Life Science

Min Sun Lee

Abstract

Enhancement of 3-dimensional positioning accuracy in PET detector for high resolution PET system

Min Sun Lee
Interdisciplinary Program in Radiation Applied Life Science
The Graduate School
Seoul National University

The positron emission tomography (PET) is a widely used imaging modality that provides biological information at the molecular level. The biological information in molecular and cellular level enables a new discovery in both pre-clinical studies and clinical cases. However, due to the fundamental limits of the spatial resolution in the PET system, the effectiveness of PET is limited when diagnosing small-sized lesions. Hence, improving the spatial resolution in PET is important for the maximization of the diagnosing power of the PET system.

In this thesis, studies on enhancing 3-dimensional (3D) positioning accuracy in PET detector for the high resolution PET system were conducted and presented. The depth-of-interaction (DOI) encoding/decoding and inter-crystal scattering (ICS) event identification technologies were developed and evaluated in the PET

detector and system level.

Firstly, the DOI encoding PET detector was developed and detector performances were evaluated. Maximum-likelihood estimation based DOI decoding methodology was developed and optimization studies in several aspects were conducted to achieve the high *z*-axis positioning accuracy. Secondly, based on the developed DOI encoding/decoding technologies, a prototype DOI PET system was developed and system-level performances were evaluated. Phantom and animal imaging studies were conducted to evaluate imaging performances of the prototype DOI PET system. The proposed DOI encoding/decoding technology was successfully demonstrated at the system level showing its feasibility for the high resolution PET application. Thirdly, a new ICS event identification method was proposed: a new technology of classifying and identifying ICS events in PET detectors with light sharing design, which was not feasible with existing technologies. The proposed method was validated by conducting simulation and experimental studies. By recovering identified ICS events, which is improving *x*- and *y*-direction positioning accuracy in the PET detector, improvement in the PET intrinsic spatial resolution was observed. In conclusion, the technologies developed in this thesis enhanced the spatial resolution of the PET system.

Keyword : Positron Emission Tomography, PET detector, High resolution, Depth-of-interaction, Inter-crystal scattering
Student Number : 2012-21778

Table of Contents

List of Figures

List of Tables

Chapter 1. Introduction

1.1. Background

Positron emission tomography (PET) is a widely used diagnostic imaging modality in both preclinical studies and clinical practices. PET visualizes biological information at the molecular level. The biological information at molecular and cellular level enables not only the diagnosis in a wide range of disease states, but also the evaluation of new drugs, imaging probes, and disease models (*1*-*5*). PET detects a pair of 511-keV annihilation gamma-rays that are emitted from the positron-emitting radiopharmaceuticals distributed in a patient body. A pair of gamma-ray is coincidently detected by PET detector elements, and a line-of-response (LOR) is generated by connecting two detector elements assuming that activity is distributed uniformly along the LOR. Finally, tomographic images are reconstructed based on the LORs.

The state-of-art clinical PET system provides 3 – 4 mm spatial resolution (*1*), which is not so good compared to anatomical imaging devices such as Computed tomography (CT). With the low image resolution, the quantitative accuracy of PET and lesion detectability decreases due to partial volume effects and spill-over-ratios (*5*, *6*). With the high image resolution, it is possible to acquire precise spatial information of radiopharmaceutical distributions which improves lesion detectability (*2*).

Therefore, PET image with good spatial resolution and image quality is

important for the precise diseases diagnosis. The ideal spatial resolution of PET system when a point source is located at the center of PET system can be expressed as below **Equation 1-1**. The ideal spatial resolution, which is also well known as intrinsic spatial resolution, is represented in FWHM (full width at half maximum) and determined by the width of scintillation crystal element (d) of the PET detector (*4*).

$$\text{FWHM} = \frac{d}{2} \quad [mm] \tag{1-1}$$

Not only the scintillation crystal size, various factors affect PET spatial resolution which are positron range, acollinearity, crystal decoding error, inter-crystal scattering effect, depth-of-interaction effect, and reconstruction algorithm. By considering above factors, the practical PET system resolution can be expressed as the below **Equation 1-2** (*4*),

$$\text{FWHM} = 1.25\sqrt{\left(\frac{d}{2}\right)^2 + s^2 + (0.0044R)^2 + b^2 + c^2 + \frac{(12.5r)^2}{r^2 + R^2}} \tag{1-2}$$

that is represented as the sum of quadratic sums of intrinsic resolution ($d/2$), positron range (s), acollinearity ($0.0044R$), crystal decoding error (b), and depth-of-interaction effect ($\frac{1.25r}{\sqrt{r^2+R^2}}$). The multiplicative factor of 1.25 due to reconstruction algorithm, and R is the radius of the PET system.

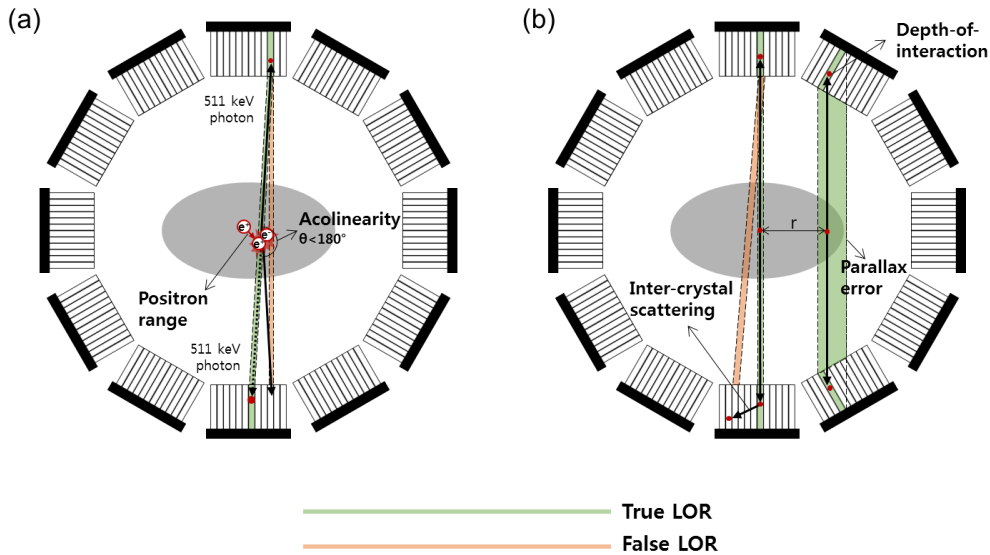

Figure 1-1 (a) Positron range and acolinearity in PET system. (b) Parallax error due to depth-of-interaction effect and inter-crystal scattering event in PET system.

Positron range and acolinearity

The positron range and acolinearity are the factors that arise from physical properties of PET principles (*6*). When a positron is ejected from a nucleus, it travels a certain distance based on its kinetic energy. The kinetic energy of positron depends on the parent radionuclides, and by traveling some distance from the position that radioactive decay took position blurring is introduced as shown in **Figure 1-1(a)**. When a thermalized positron collides with an electron, a positronium (a complex of positron and electron) is formed and annihilated photons are subsequently emitted back-to-back satisfying energy-momentum conservation law. However, the positronium has non-zero residual kinetic energy and results in slight acolinear annihilation photon emission as shown in **Figure**

1-1(a). These two factors may lead to false LOR positions that degrade image resolutions and qualities. I would like to point out that these two factors are the underlying physical properties of PET that cannot be solved with practical solutions.

Crystal decoding error

The crystal decoding error is the error due to the optical coupling of more than one scintillation crystals with photo detector channels. In order to reduce the number of electronic channels, most of PET system uses n-to-1 optical coupling between scintillation crystal and photo detectors. Even though multi-channel photo detectors with smaller effective sensor area is developed, still most of PET system uses crystal decoding (*7*). This crystal decoding is usually imperfect compared to 1-to-1 coupling of scintillation crystal and photo detectors and degrades spatial resolutions. This term is demonstrated as $d/3$, which is determined empirically.

Depth-of-interaction effect

The depth-of-interaction effect is caused by the oblique photon incidence in the detector at the peripheral PET field-of-view (FOV) and in long axial FOV PET scanners. Since the 2- to 3cm-thick scintillation crystal is required to efficiently stop the 511-keV gamma-ray, blurring in LOR is observed since we do not know depth of gamma-ray interaction position in PET detectors. When the

source is located far from the center of FOV, these depth-of-interaction effects become more severe leading to the LOR blurring as shown in **Figure 1-1(b)**. This is radial blurring is called parallax error and the spatial resolution is degraded as the distance from the center (r) increases in the radial direction (*8, 9*).

Inter-crystal scattering effect

When a 511-keV gamma-ray undergoes Compton scattering and deposits a portion of its energy in more than one crystal elements in a PET detector, it is referred as inter-crystal scattering event. Events that undergo inter-crystal scattering cause mispositioning of gamma interaction position resulting in false LORs as shown in **Figure 1-1(b)**, and false LORs lead to degradation in image resolution and contrast. Inter-crystal scattering is more frequently observed in high resolution PET application with small crystal size.

1.2. Purpose of this study

As described in section **1.1**, the fundamental lower bound of the PET spatial resolution is mainly determined by the crystal element size (d), and it is degraded by the mispositioning of gamma-ray interaction position caused by several factors. Hence, by improving the positioning accuracy of gamma-ray interaction positions in PET detectors, we can improve the PET system spatial resolution.

The aim of this thesis is to enhance the 3-dimensional (3D) positioning

accuracy in PET detector for the high resolution PET system. As the means of 3D positioning accuracy improvement, depth-of-interaction encoding/decoding and inter-crystal scattering event identification technologies were developed. The strategies are to improve *z*-direction positioning accuracy by using depth-of-interaction information, and improve *x*- and *y*- direction positioning accuracy by using inter-crystal scattering event information.

In Chapter 2, depth-of-interaction information encoding PET detector was developed and optimized, and detector-level performances were evaluated (*10*). The proposed depth-of-interaction encoding PET detector is a novel design providing low-cost depth-of-interaction measurement. In this thesis, a new depth-of-interaction decoding methodology was introduced, and several optimization studies were performed for the high *z*- direction positioning accuracy. In Chapter 3, a prototype PET system with depth-of-interaction measurement capability was developed (*11*) based on the detector technologies presented in Chapter 2. Here, a prototype PET system was developed and PET system performances were evaluated. Several imaging studies were performed to see the impact of the proposed depth-of-interaction encoding/decoding technologies at the system level in terms of image resolution and quality. In Chapter 4, inter-crystal scattering event identification method was proposed and its performance was evaluated based on the simulation study and finally validated based on the experimental study.

Chapter 2. Depth-of-interaction PET detector

2.1. Background

As discussed in **Chapter 1**, one of major factors that deteriorates image resolution and uniformity in PET system is the depth-of-interaction (DOI) effect, where DOI is the interacted depth position of in a long scintillation crystal. Due to the DOI effect, the parallax error is observed, which is a loss of resolution in the peripheral region of the FOV owing to mispositioning of the LOR (**Figure 1-1(b)**). This parallax error is more severe in PET scanners with a small FOV and relatively long crystal elements and in PET scanners with a long axial FOV. The main way to reduce the parallax error is to use the detectors with DOI measurement capabilities. By using DOI information in detectors, the parallax error can be reduced and thus the PET system can achieve fine resolution over the imaging FOV (*8, 9, 12*).

Various DOI measurement methods have been proposed, including discrete DOI measurements using multiple layers of crystals and/or photosensors (*13-15*) and continuous DOI measurements using two or more readouts (*16, 17*), light sharing within a crystal array (*18-20*), and statistical methods using monolithic crystals (*21*). However, many of these approaches have high manufacturing costs because of the large number of crystal elements, photosensors, and/or readout channels to deal in the electronics (*22*). Hence, it is very important to develop DOI measurement methods that have reduced manufacturing cost and complexity

while maintaining the DOI-encoding accuracy (*18*, *21*, *23-25*).

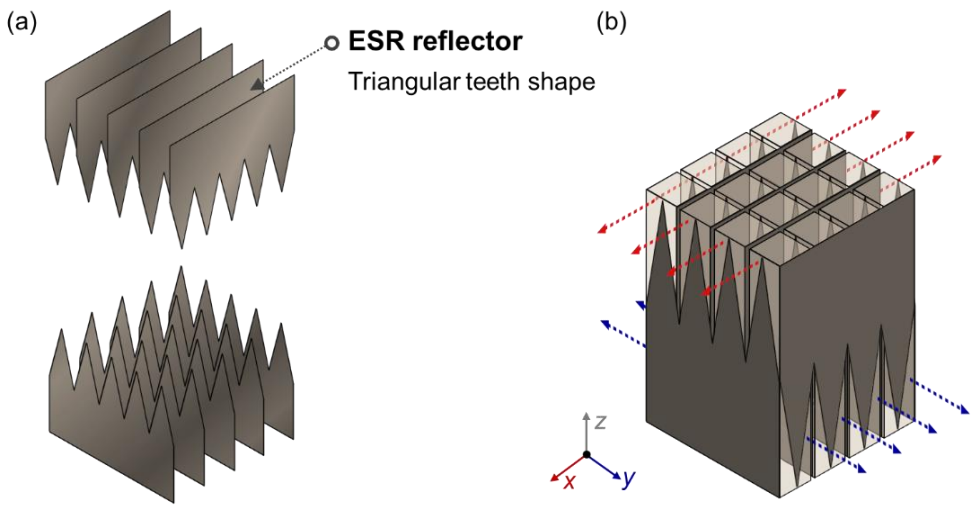

Figure 2-1 Concept of the continuous DOI-encoding PET detector. (a) Triangular teeth shape reflectors cross each other, (b) and crystals were inserted in the reflector grid.

Previously, our group proposed a novel PET detector concept to measure continuous DOI information from a single-layer crystal array using a single-ended readout (*18*). The principle of the proposed continuous DOI-encoding detector (referred to as the "cDOI detector") is that the light spreading within the crystal array partially covered with reflectors having triangular teeth crossed over itself (**Figure 2-1(a)**). Because of the reflector configuration, different light dispersion patterns are attainable along the *x*- and *y*-directions depending on the gamma-ray interaction depth (*z*) (**Figure 2-1(b)**). Different two-dimensional light dispersion patterns for different DOI positions are observed from the detector response function of photosensors. Consequently, DOI information is

encoded through different light dispersion patterns that are recorded as detector responses. The proposed method has the novelty in that realization of low-cost high performance DOI measurements.

In this study, continuous DOI-encoding PET detector was developed and new DOI-decoding methodology was suggested to acquire high depth (*z*-direction) positioning accuracy. Several optimization studies were performed based on the simulation and experiments to acquire good detector performances. Finally, the detector-level performances were evaluated and reported.

2.2. Materials and methods

2.2.1. Continuous DOI-encoding detector

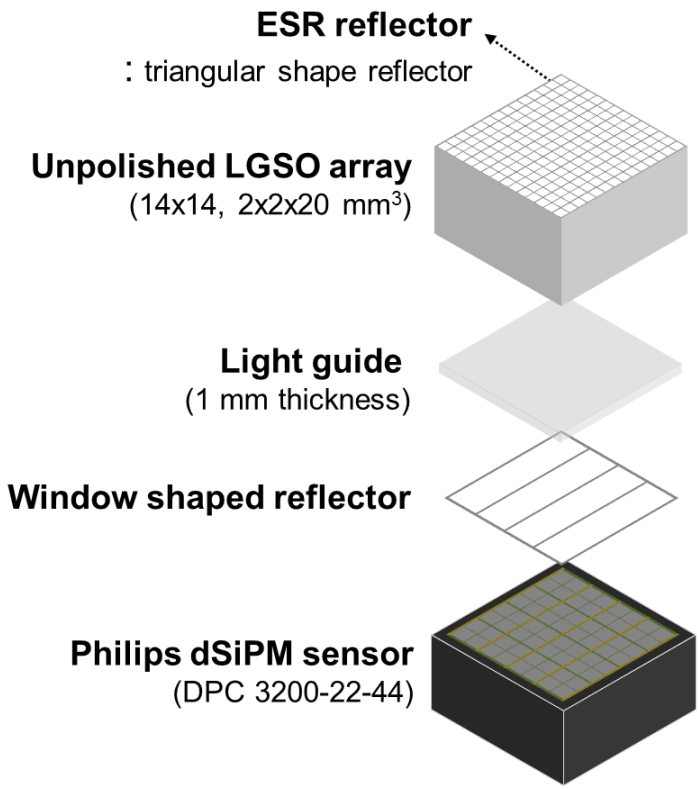

Figure 2-2 Components of cDOI-dSiPM detector.

The DOI-encoding detector was developed using a Philips digital silicon photomultiplier (dSiPM) sensor (DPC-3200-22-44, Philips Digital Photon Counting) coupled with a single-layer pixelated scintillation crystal as illustrated in **Figure 2-2**. The crystal array consisted of 14×14 chemically unpolished LGSO crystals ($Lu_{1.9}Gd_{0.1}SiO_5$:Ce; Hitachi Chemical, Tokyo, Japan) with a pixel size of 2.0×2.0×20 mm^3. Each crystal was wrapped with a triangular teeth shaped

enhanced specular reflector (ESR) polymer (3M, St. Paul, MN, USA). A light guide with a thickness of 1 mm was inserted between the sensor and crystal array to efficiently spread light across the pixels. Additionally, a window-shaped reflector was inserted between the sensor and light guide to reduce the light loss in the 0.8-mm-wide dead spaces between pixels. All components were optically coupled using optical grease (BC-630; Saint-Gobain, Paris, France).

2.2.2. DOI decoding methodology

Previously, DOI information was extracted from a 2-D detector light distribution using a simple arithmetic function of detector response parameters (*24*). In this study, I suggested to use a more consistent and systematic DOI decoding method to for the depth positioning with higher accuracy. Thus I adopted maximum-likelihood (ML) estimation-based positioning with a statistically modeled detector response (*19, 26*) for the depth decoding. This ML-based method is expected to be more consistent and systematic since it exploits the overall response of a detector system including the intrinsic characteristics of individual crystal elements and front-end and readout electronics.

Since the detector response follows a statistical process, each 8×8 detector response was modeled as a Gaussian model. Each 8×8 detector response has characteristic values of mean (μ) and standard deviation (σ), at different DOI positions $\vec{z}$ ($\vec{z}$ = 2, 6, 10, 14, and 18 mm); hence, μ and σ can be represented as functions of $\vec{z}$. The depth-dependency of detector response characteristics of

cDOI detector was also experimentally validated and this is discussed in the results section.

The likelihood function $L(\vec{\boldsymbol{z}}|\boldsymbol{S})$ of the detector signal $\boldsymbol{S} = [s_1, s_2, \dots, s_{64}]$ of a single gamma event at depth position $\vec{z}$ was composed of the product of independent Gaussian functions at the i^{th} channel as **Equation 2-1**. We denote $\mu_i(\vec{\boldsymbol{z}})$ and $\sigma_i(\vec{\boldsymbol{z}})$ as the mean and standard deviation at i^{th} channel, which are functions of the depth. Finally, the DOI position z can then be estimated from an ML estimate ($\hat{\vec{\boldsymbol{z}}}_{ML}$) which maximizes the likelihood function as described in **Equation 2-2**.

$$L(\vec{\boldsymbol{z}}|\boldsymbol{S}) = \prod_{i=1}^{64} \frac{1}{\sigma_i(\vec{\boldsymbol{z}})\sqrt{2\pi}} \exp\left(-\frac{(s_i - \mu_i(\vec{\boldsymbol{z}}))^2}{2\sigma_i^2(\vec{\boldsymbol{z}})}\right) \qquad \textbf{(2-1)}$$

$$\hat{\vec{\boldsymbol{z}}}_{ML} = \arg\max_{\forall \vec{z}} L(\vec{\boldsymbol{z}}|\boldsymbol{S}) \qquad \textbf{(2-2)}$$

Two look-up tables consisting of the means and standard deviations of the detector responses were generated for training data using 70% of depth calibration data for each 3D interaction position. The remaining 30% were used to test the likelihood function. Finally, ML estimate ($\hat{\vec{\boldsymbol{z}}}_{ML}$), which is the estimated interaction position, was obtained by maximizing the likelihood function $L(\vec{\boldsymbol{z}}|\boldsymbol{S})$. Here, I used the *DOI positioning accuracy*, which is the percentage of correctly acquired DOI estimates at each known depth, as an indicator of DOI performance.

2.2.3. DOI detector optimization study

2.2.3.1 Digital readout vs. analog readout

In the proposed DOI decoding method, it is important to acquire precise information from detector. The individual detector signal readout is one approach to acquire accurate detector responses, but it is challenging because complicated data acquisition (DAQ) system is required for the conventional SiPMs with analog readout. The SiPM with digital readout, recently developed sensor from Philips Digital Photon Counting, is a SiPM operated in all-digital operation mode and provides easy individual signal readout without complicated DAQ system (*27*).

Two different readout schemes of SiPM were simulated to find the proper readout scheme for the DOI measurement: (a) Scheme 1: SiPM with digital individual readout and (b) Scheme 2: SiPM with analog row and column sum readout, which is a typical readout method used in analog PET detectors. The scintillation pulses were generated using a Monte Carlo simulation with individual scintillation photon tracking using GATE (Geant4 Application for Tomographic Emission) v.6.2 toolkit (*28*). The SiPM characteristics, SiPM noises including dark count (DC), after pulse (AP), and optical crosstalk (OC), analog circuit electronic noise, and complexity of readout circuit for DOI-encoding were simulated comprehensively by using MATLAB software. Two schemes were simulated to have the same SiPM characteristics including noises except for analog electronic noises.

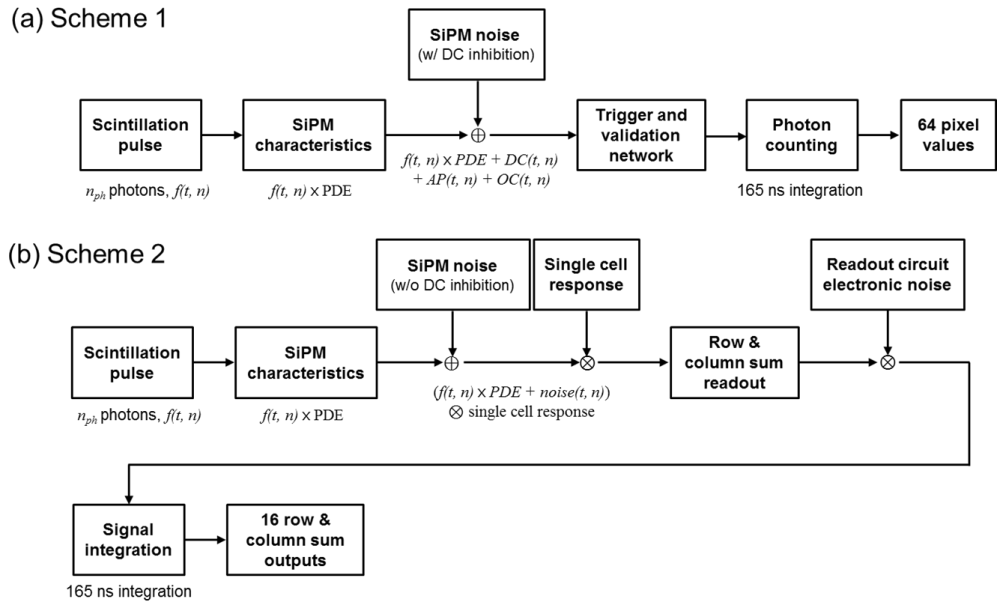

Figure 2-3 Simulation study conducted to see the effect SiPM signal readout scheme on the DOI performance. (a) Scheme 1: SiPM with digital readout and (b) Scheme 2: SiPM with analog readout.

The simulation study was performed with following procedure (**Figure 2-3**). In Scheme 1, 10% of the highest dark count cells in the 64 pixels were inhibited as the real experiment and the photon detection efficiency (PDE) value is decreased respectively. The trigger and validation threshold were applied in the same manner as the real sensor with the photon count threshold used in the real experiments. Then the photon counts were integrated for 165 ns for each pixels and finally 64 pixel values were acquired to analyze the DOI performance (**Figure 2-3(a)**). In Scheme 2, noise added scintillation pulses were convolved with the single cell response (*29*). Then each 64 scintillation pulse that exceeded the threshold (same with Scheme 1) went through the row and column sum

readout and reduced to 16 pulses. The electronic noises arisen from readout circuit with the RMS value of 850 μV was added to 16 output signals. The RMS noise was measured from our in-house developed 16-Ch row and column sum readout circuit. Each 16 scintillation pulse were integrated within 165 ns to analyze the DOI performance (**Figure 2-3(b)**).

2.2.3.2 dSiPM sensor operating parameter

The dSiPM provides configurable data acquisition network, so it is important to find the optimal dSiPM operating parameters for the successful implementation of the cDOI measurement and for the good detector performances. Here, various sensor configurations and system settings were tested to find the optimal operation condition for the good detector performance. Several parameters were considered: the acquisition coincidence time window, the temperature of the experimental setting, and the trigger and validation scheme. Parameters were determined to obtain sufficiently high *full-tile triggering ratio*, high *effective event ratio*, good energy resolution, and clear crystal identification.

After the parameter optimization, detector performances were evaluated. A full-tile NL configuration in dSiPM was used which enables all 8×8 pixel values acquisition and thus examine the light distribution of the cDOI detector. The validation length was set to 40 ns, and the integration length was set to 165 ns. The 10% of cells with the highest dark count in the sensor were inhibited. All experiments were performed with a front-on irradiation scheme using a ^{22}Na

point source (~17.5 μCi) as depicted in **Figure 2-4(a)**. All results were analyzed for the same number of coincidence events (1.5 M).

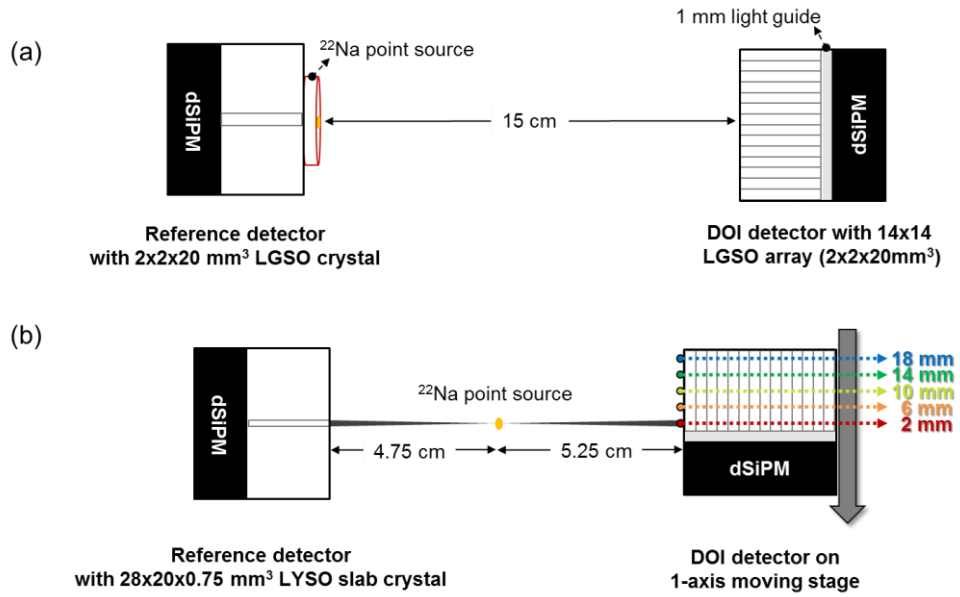

Figure 2-4 Experimental setup used in this study. (a) Front-on irradiation scheme and (b) side-on irradiation scheme.

Acquisition coincidence time window

The acquisition coincidence time window dictates the operation of the full-tile NL configuration in dSiPM, which is essential in our DOI measurement. Here, three acquisition coincidence time windows of 30, 35, and 40 ns were considered. The final acquisition coincidence time window was determined by measuring the *full-tile triggering ratio* that is defined as the number of events that underwent full-tile NL to the total number of events.

Temperature

A temperature optimization study was carried out to find the suitable temperature range that did not perturb the performance of the cDOI detector. The temperature was controlled by a temperature control box (CT-BDI150, Coretech, Korea). Investigated temperatures were 0, 5, 10, 15, and 20 ℃. The *event rate*, *effective event ratio, full-tile triggering ratio*, energy performance, and photo peak position were investigated to find the proper temperature range. The *effective event ratio* is the ratio of the number of events entered within a ±25% photo peak window to the total number of events; the ratio represents the number of valid 511 keV gamma-ray events.

Photon count threshold

The dSiPM offers configurable photon count threshold. The photon count threshold was optimized by examining the detector performances of all possible trigger and validation schemes, 16 cases in total. Each combination of trigger and validation schemes offers a different photon count threshold. With low trigger and validation schemes, it is possible to obtain time information from early-stage photons leading to good time resolution. However, the probability of false event acquisition and the dead time increase (*30*). With high trigger and validation schemes, it is possible to suppress false triggering at the expense of poorer time resolution (*27*). To determine the optimal trigger and validation configuration for the cDOI detector, the *effective event ratio* and *full-tile triggering ratio* were

evaluated. Measurements were conducted with full-tile neighbor logic and a coincidence time window set to 40 ns at 0 ℃.

2.2.3.3 Surface treatment

Since our DOI-encoding design is based on light sharing among crystals, the crystal surface treatment conditions play an important role in controlling light dispersion. Therefore, appropriate surface conditions are required that provide good DOI performance without detector performance degradation. Here, two types of unpolished LYSO crystal blocks with different surface roughness were tested, which was controlled by lapping the crystal surface with two abrasive grit sizes:

1) 200 grit for a rougher surface,

2) 1200 grit for a finer surface.

Experimental study was conducted as shown in **Figure 2-4(b)**, and flood histogram quality, energy resolution, and DOI positioning accuracy were evaluated to determine the appropriate surface treatment conditions.

2.3. Results

2.3.1 DOI detector optimization results

2.3.1.1 Digital readout vs. analog readout

Two different schemes of SiPM were simulated where Scheme 1 refers to SiPM with digital individual, and Scheme 2 refers to SiPM with analog row and column sum readout. DOI performance was evaluated with four different cases: 1) ideal case without any noise sources, 2) with dark count (DC) noises, 3) with dark count, optical crosstalk (OC), and after pulse (AP) noises, and 4) with DC, OC, AP, and electronic noises. The DOI performance for typical seven crystals were averaged in **Table 2-1** with DOI positioning accuracy value.

Table 2-1 DOI performance of two simulation schemes.

Simulation cases	Scheme 1	Scheme 2
Without any noise (ideal)	93.32%	85.75%
With DC noise	92.68%	87.86%
With DC + OC + AP noise	69.07%	62.54%
With DC + OC + AP noise + electronic noise	Not applied	59.29%

For every case, Scheme 1 showed the better results. Even in the ideal case without any noise Scheme 1 showed the better results, which reveals that digital individual readout offers better DOI performance compared to the analog row and column sum readout. For Scheme 2, the number of readout channel is reduced by a factor of 4 at the expense of the estimation accuracy. Furthermore, noise propagation due to channel multiplexing increases statistical uncertainty in the estimation model.

2.3.1.2 dSiPM sensor operating parameter

Three operation condition were optimized as described in section **2.2.3**. For appropriate use of the full-tile NL configuration, the acquisition coincidence time window was adjusted. The optimal choice was a 40 ns time window as described in **Table 2-2** which provides higher *full-tile triggering ratio*.

Table 2-2 Results of acquisition coincidence time window selection.

CTW setting [ns]	30	35	40
Full-tile triggering ratio	53.99	79.66	84.99

As a second study, a temperature optimization study was performed to find the tolerable temperature range that did not notably degrade performance. The temperature condition dictates the dark count and electric noise of the photosensor. An increased temperature generated false trigger events, leading to performance degradation as shown in **Table 2-3**. Therefore, a temperature range of 0−15 ℃ was acceptable and for the detector performance evaluation, the temperature was set to 0 ℃ to acquire the best performance.

Table 2-3 Results of temperature dependent detector performance evaluation for the temperature range of 0 – 20° C.

Temperature [°C]	0	5	10	15	20
Event rate [kHz]	5.30	5.56	5.62	5.77	5.99
Effective event ratio [%]	74.32	74.33	74.11	73.20	72.74
Full-tile triggering ratio [%]	80.60	76.49	70.15	61.02	47.14
Global energy resolution [%]	20.81	20.84	21.09	21.52	22.40
Photo peak position [a.u.]	2850	2850	2850	2880	2850

Finally, the photon count threshold optimization was studied by evaluating several detector parameters employing all possible trigger and validation schemes, as presented in **Table 2-4**. The table shows that *effective event ratio* of the low photon count threshold were very low, because most of the events were filtered out by the level of photon counts as unwanted events. Hence, at least validation scheme 4 was required to attain a certain *effective event ratio*. At least trigger scheme 2 and validation scheme 4 are required to satisfy both a high *full-tile triggering ratio* and high *effective event ratio*.

Table 2-4 Results of photon count threshold selection study for different trigger and validation schemes.

Effective event ratio [%]	**Trig 1**	**Trig 2**	**Trig 3**	**Trig 4**
Val 1	0.00	0.29	0.44	12.66
Val 2	1.64	3.45	5.27	16.60
Val 4	57.07	68.61	68.51	62.49
Val 8	60.96	72.78	73.15	74.32
Full-tile triggering ratio [%]	**Trig 1**	**Trig 2**	**Trig 3**	**Trig 4**
Val 1	0.32	7.82	10.50	58.74
Val 2	0.53	12.38	17.16	58.68
Val 4	8.54	61.86	66.25	75.34
Val 8	5.60	56.10	61.88	80.60

2.3.1.3 Surface treatment

The energy resolution of cDOI detector at the center crystal of crystal array, which was averaged over all depths, was 10.78% for the 200-grit and 9.72% for the 1200-grit crystal array. The DOI-dependent shift of the primary peak position in energy spectra was less severe in the 1200-grit crystal array (**Figure 2-5(a), (b)**). The average DOI positioning accuracy at the center crystal obtained by MLE was 68.55% and 64.71% for the 200- and 1200-grit crystal array, respectively. The DOI performance was fairly uniform for 18 crystal positions at the center row of crystal array and the average DOI positioning accuracy was 60.97% and 60.67% for the 200- and 1200-grit crystal arrays, respectively, as shown in **Figure 2-5(c)**. The quality of two flood histograms was almost equivalent. Accordingly, I decided to use 1200-grit-lapped unpolished crystals for the prototype system.

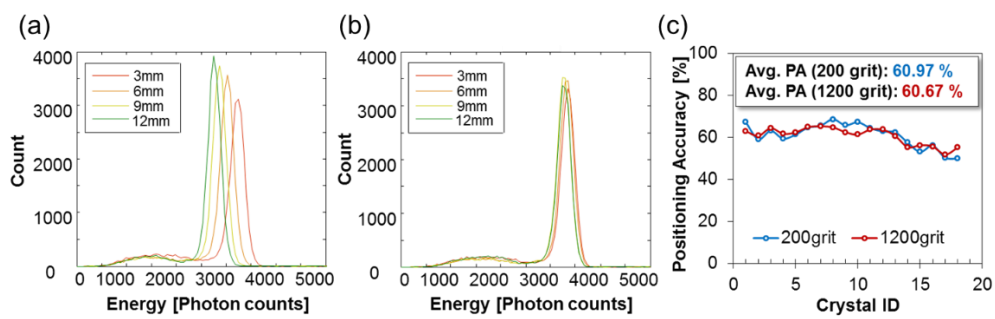

Figure 2-5 Effect of crystal surface treatment on cDOI detector. Energy spectra for the (a) the 200-grit crystal and (b) the 1200-grit crystal. (c) DOI positioning accuracies for the 200-girt and 1200-grit crystals for 18 crystals at the center row.

2.3.2 DOI detector performances

2.3.2.1 Detector performance

One of the advantages of cDOI detector is its simple crystal identification since the detector is composed of pixelated crystals. A flood histogram was generated by a weighted mean calculation of 8×8 pixel values. **Figure 2-6(a)** illustrates that crystals were clearly resolved except for crystals located at the edges. The merging of crystals at two edges is due to the configuration of our cDOI reflector design.

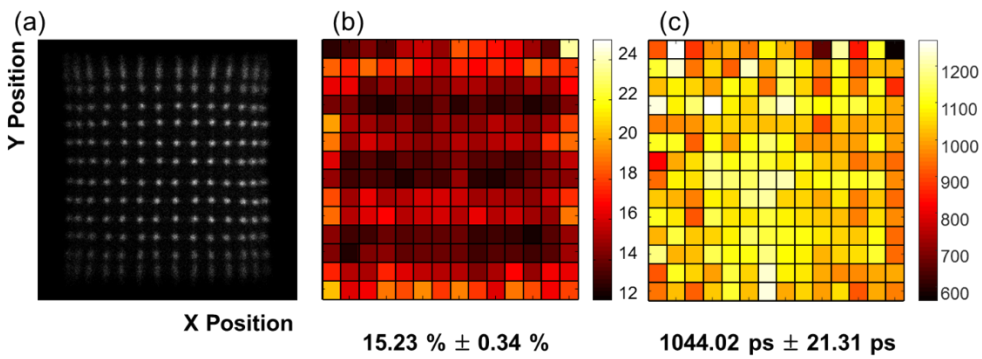

Figure 2-6 cDOI detector performances. (a) Flood histogram. (b) 2D energy resolution histogram. (c) 2D global time resolution histogram.

The global energy performance was observed as a 2-D energy resolution histogram of each 14×14 crystal with a corrected photo peak position as shown in **Figure 2-6(b)**. The global energy resolution was 15.23% ± 0.34% averaged over all crystals. The global time performance was examined as shown in **Figure 2-6(c)**, which presents a 2-D coincidence time resolution histogram for each crystal. The global time resolution averaged over all crystals was 1069.34 ± 15.98

ps. The time performance was not so good because the highest photon count threshold was used in this study. Time skew correction was applied for this result.

2.3.2.2 DOI performance

Detector response

Detector responses were initially observed to evaluate the characteristics of the cDOI detector and to confirm its DOI-encoding capability. The normalized 8×8 pixel values of the detector were plotted as 2-D graphs for five depth positions. **Figure 2-7** shows depth-dependent detector responses at several different crystal positions. Center crystal, off-center crystals on the central pixels, off-center crystals on the off-center pixels were chosen in the lower-right of crystal array to examine the light distribution patterns through depth positions (**Figure 2-7(a)**). For every crystal positions, different light distribution pattern was observed at five depth positions. (**Figure 2-7(b)**)

First of all, the cDOI detector showed the depth-dependency. At the 2 mm depth position, higher peaks were observed with rapid gradient, while the 18 mm depth position showed lower peaks with slow gradient. These results illustrate that the cDOI detector has good DOI-encoding capability. Secondly, detector response has the crystal position dependency. The center crystal placed on the pixel center (crystal #1) showed relatively lower peak values in normalized detector responses because of the even light spreading over the entire crystal array. The off-center crystals placed on the pixel center (crystal # 2, 4, 6) showed

higher peak values in detector responses when moving further from the center of the crystal array. In case of off-center crystals placed on the off-center pixels (crystal # 3, 5) showed slightly flat detector responses compared to crystals on the pixel center. Crystals at different positions showed different light distribution patterns, but there were no prominent changes in positioning accuracies over all crystals depending on their crystal positions.

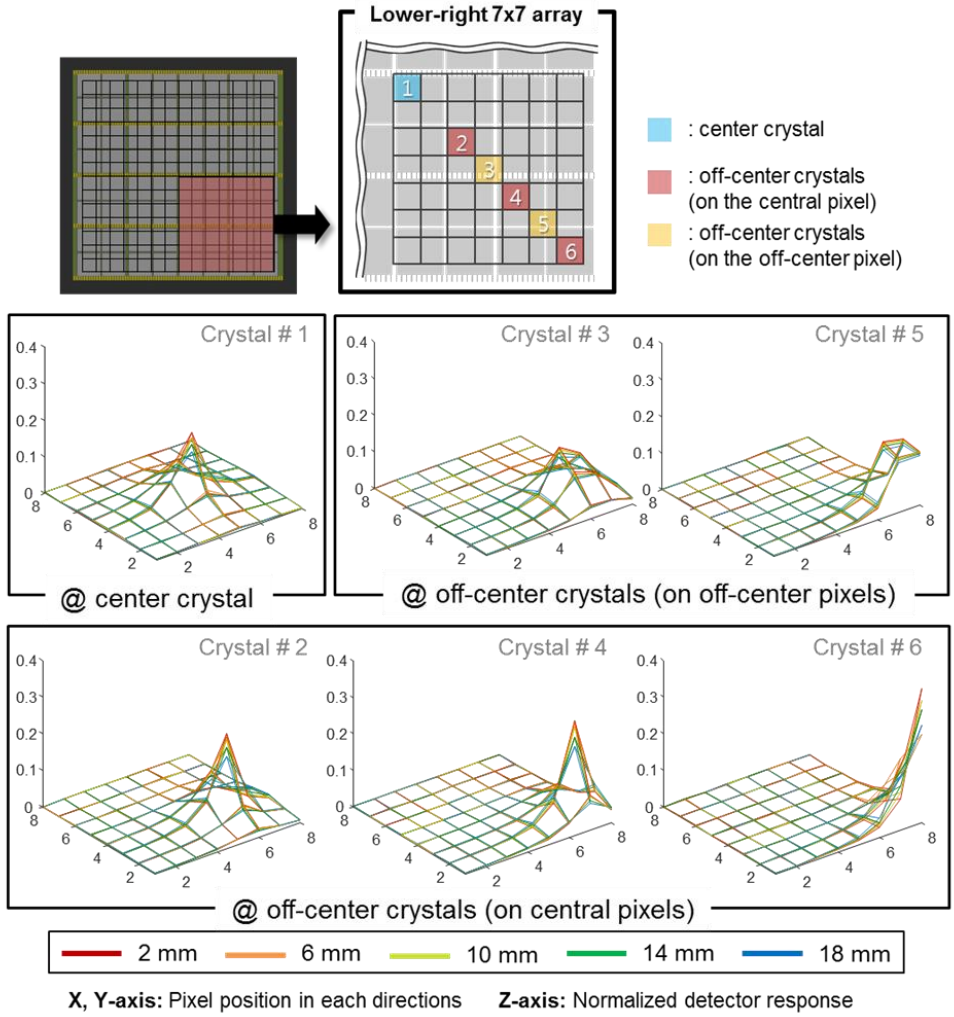

Figure 2-7 Depth-dependent detector responses for six different crystal positions.

DOI positioning accuracy

Proceeding from the previous section, the ML estimation method was applied to decode DOI information from side-on irradiation experiment data with the estimated DOI positions at each irradiation depth, the *DOI positioning accuracy* was calculated to assess the DOI decoding capability.

The histograms in **Figure 2-8** illustrate the ML-estimated DOI positioning accuracy for each known irradiation depth at the center crystal. The estimated DOI position along the x-axis corresponds to five DOI positions, 2, 6, 10, 14, and 18 mm. In the case of 2-mm irradiation data (**Figure 2-8(a)**), the positioning is estimated with 78.59% accuracy (red bar). DOI positions were also estimated well at other irradiation positions with a positioning accuracy of 74.22% ± 6.77% averaged over all depths.

DOI positioning accuracy at the center crystal is summarized in **Table 2-5**. The ML-estimated result shows that the cDOI-SiPM detector decodes DOI information with high accuracy at the exact position. When considering an error range of ±1 DOI positions, almost all events were estimated correctly with 96.29% average positioning accuracy over five irradiation positions. By converting the average DOI positioning accuracy of 74.22% into a DOI resolution with millimeter units, the average DOI resolution at the center crystal was obtained as 4.67 mm.

Figure 2-8(f) shows DOI positioning accuracies of the whole crystal array. The average DOI positioning accuracy for all 196 crystals was 63.97% ± 4.64%

that corresponds to DOI resolution of 4.82 mm ± 0.25 mm. We observed a slight degradation of accuracy at the back part of the crystal array because of the beam broadening.

Table 2-5 ML-estimated DOI positioning accuracy at the center crystal

Irradiation depth	Positioning accuracy [%] (@ estimated DOI position)					Regarding ± 1
	2 mm	6 mm	10 mm	14 mm	18 mm	
2 mm	78.59	16.09	1.94	0.97	2.41	94.68
6 mm	11.10	73.20	12.07	1.47	2.16	96.37
10 mm	1.54	11.31	70.19	11.49	5.46	93.00
14 mm	0.90	0.25	10.09	65.98	22.77	98.85
18 mm	0.75	0.07	0.61	15.45	83.12	98.56

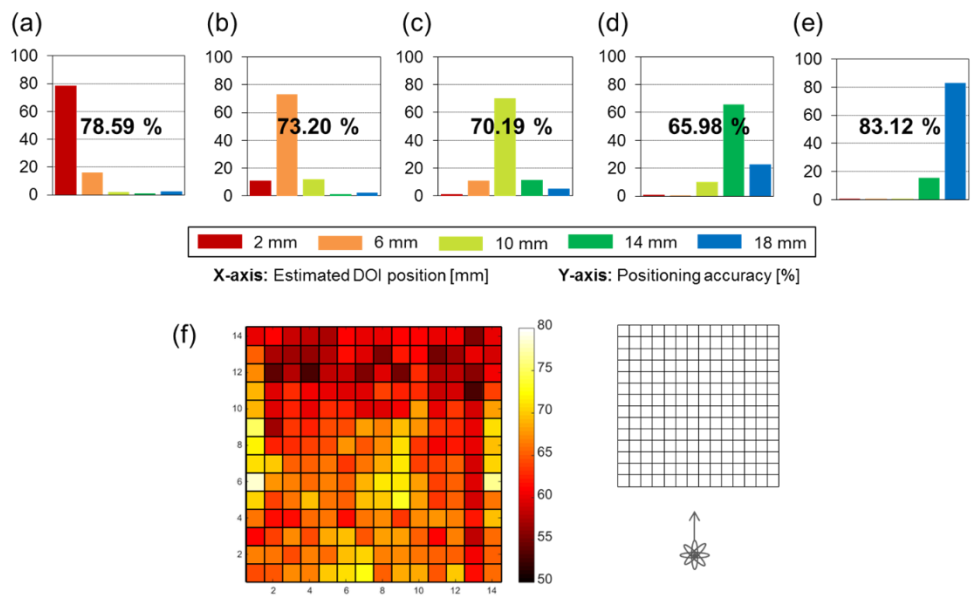

Figure 2-8 Positioning accuracy histogram at the center crystal at five irradiation positions (a) 2 mm, (b) 6 mm, (c) 10 mm, (d) 14 mm, and (e) 18 mm.
(f) Positioning accuracy map for the whole crystal array with corresponding direction.

2.4 Discussion

Using a dSiPM as a photosensor for our DOI measurement had several advantages over using analog devices. The most important benefit was the simplification of the individual pixel readout, which increased the accuracy of the light distribution measurement and offered flexibility in investigating the optimal DOI estimation scheme. By combination of dSiPM technology and the proposed ML-based DOI positioning, we obtained high DOI positioning accuracy.

After several optimization processes including optimization of the acquisition coincidence time window, temperature, and photon count threshold, I found optimal conditions for operating our cDOI-dSiPM detector. I successfully developed a cDOI-dSiPM detector that provided good crystal identification and good global energy resolution. Timing resolution was poor because we applied the highest photon count threshold in the experiment. At the center crystal, an energy resolution of 10.21% ± 0.15% and time resolution of 1198.61 ± 39.70 ps were obtained. The average DOI resolution at the center crystal was 4.67 mm, which was reasonably good, and the DOI resolution was uniform along a row of crystals with slight degradation at the edges. I thus concluded that the prototype of the cDOI-dSiPM detector shows promise as a fine-resolution and high-sensitivity PET detector that is compatible with magnetic resonance imaging.

Chapter 3. Depth-of-interaction PET system

3.1. Background

Based on the results in **Chapter 2**, a prototype DOI PET system was developed for the proof-of-concept evaluation of the proposed DOI-encoding method in system level and showed its feasibility through phantom and small animal experiments.

3.2. Materials and methods

3.2.1. DOI-encoding PET detector

For each cDOI detector, dSiPM was optically coupled with 18×18 array of unpolished LYSO crystal (Crystal Photonics Inc., FL, US) with the size of 1.47×1.47×15 mm^3 (**Figure 3-1(a)**). As the results from the crystal surface treatment study, we used unpolished crystal with 1200-grit lapping (section **2.3.1.3**). Crystals were wrapped with triangular teeth shaped ESR. One-mm thick light guide was inserted between LYSO crystal array and dSiPM for the efficient light sharing, and window shaped reflector was used to reduce the light loss due to dead spaces between dSiPM pixels (**Figure 3-1(a)**). The specification of dSiPM is described in **Table 3-1**.

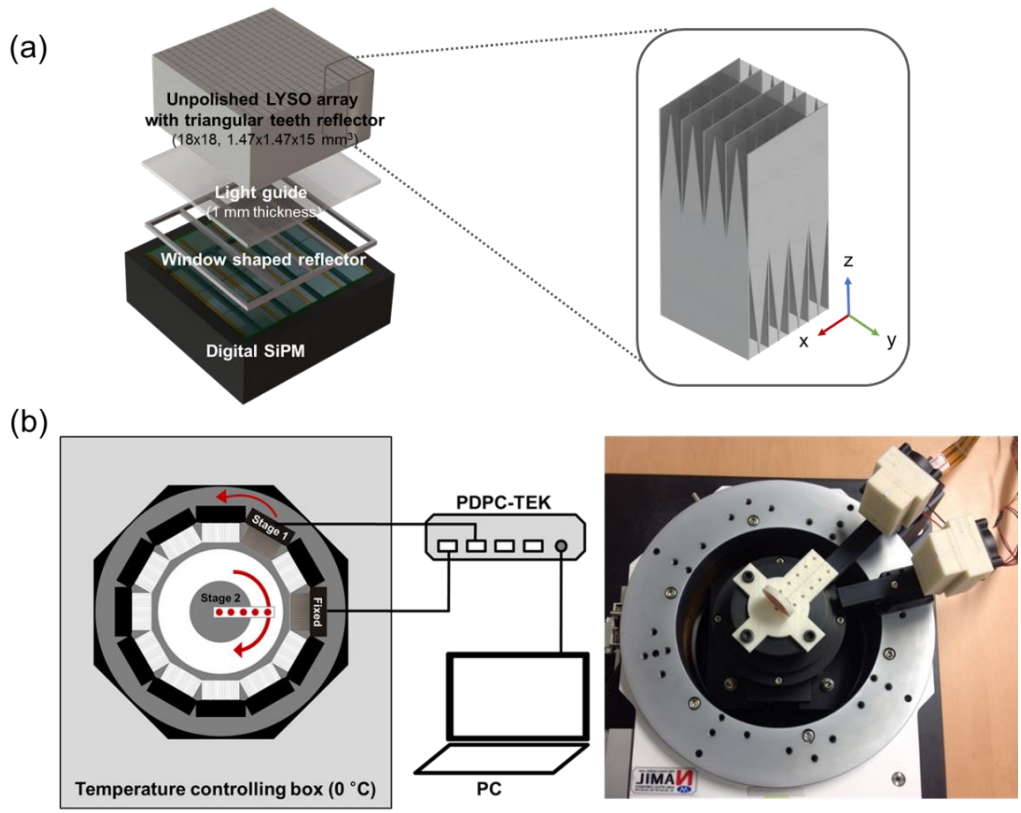

Figure 3-1 (a) Design and components of the cDOI PET detector used for the prototype system. (b) Prototype cDOI PET system consisting of two cDOI PET detector modules placed on two motorized rotation stages.

3.2.2. Prototype PET scanner

A pair of cDOI PET detector was used in this study to demonstrate a 12-block ring PET system with a diameter of 11.15 cm, and detector was fixed on the base plate, while the other one and object were rotated on the two motorized rotation stages (Namil Optical Instruments Co., Incheon, Korea) as shown in **Figure 3-1(b)**. The detector on stage 1 rotated with 30° step size at every possible detector configurations and the object on stage 2 rotated with 30° step size over imaging FOV to cover all possible LORs for the proper image reconstruction.

Data acquisition process was managed by Philips Digital Photon Counting Technology Evaluation Kit (PDPC-TEK) connected to PC. Since the dSiPM sensor offers configurable trigger and validation logic and data acquisition protocol, I used the optimized sensor configuration to acquire the good detector performance as following: trigger level 2, validation level 8, validation length 40 ns, integration length 165 ns, full-tile neighbor logic, and 10% of dSiPM cells with highest dark count rate inhibition. As shown in **Figure 3-1(b)**, the experiment setup was placed inside the temperature control box set to 0℃ for the constant temperature and dark count noise suppression.

Table 3-1 Specification of prototype cDOI PET system

Parameter	Value
Crystal	
Scintillation mateirals	LYSO
Crystal size (mm^3)	1.47×1.47×15
Crystal pitch (mm)	1.57
Crystal array size	18×18
Digital SiPM (DPC-3200-22-44)	
Pixel size (mm^2)	3.2×3.8775
No. of SPADs/pixel *	3200
No. of pixels/sensor	64 (8×8)
PDE (%) †	40
Virtual Ring System	
Face-to-face distance between detectors (cm)	11.15
No. of crystal rings	18
No. of crystals/ring ‡	216
Total no. of crystals§	3,888
Axial FOV (cm)	2.83

* SPAD: Single Photon Avalanche Diodes
† PDE: Photon Detection Efficiency
‡ No. of crystal/ring: number of crystals in one ring
§ Total no. of crystals: total number of crystals in the prototype system

3.2.3. Detector performance evaluation

In order to assess performances of two cDOI detectors, coincidence measurement was conducted using 0.7 MBq ^{22}Na point source. Peak-to-valley ratio of flood histogram, energy resolution, and DOI resolution were evaluated and reported in this study.

Flood histograms were generated by plotting two-dimensional histogram of gamma-ray interaction position obtained by the weighted mean of 64 pixel values. Peak-to-valley ratio was evaluated to assess the quality of flood histogram. Energy spectra were generated by summing 64 pixel values and energy photopeak correction was applied. Energy resolutions were reported by measuring full-width at half-maximum (FWHM) of each spectrum.

To quantify the DOI decoding performance of proposed DOI detector, the positioning accuracy was calculated using depth calibration data, which is the percentage ratio of correctly obtained MLE-based position estimates at each known position. MLE-based positioning accuracy reported in this study is the average over four depths. Two different strategies for DOI estimation were compared:

1) Simultaneous ML estimation of crystal position (x, y) and depth (z)

2) 2D center of mass (flood histogram) based estimation of crystal position (x, y) and 1D ML estimation of depth (z), which were used in the previous study (**Chapter 2**).

Finally, the DOI resolution was reported by converting positioning accuracy

of the first method (3D estimation) into millimeter units. All detector performances reported in this study is averaged over all 324 crystals.

3.2.4. Spatial resolution measurement

Spatial resolution of the prototype system was measured based on National Electrical Manufacturers Association (NEMA) NU 4-2008 protocol (*31*). Data was acquired using a 0.7 MBq ^{22}Na point source embedded in a 1-cubic-cm acrylic cube. Measurement was conducted at the axial center of FOV at the following radial distances from the center: 0, 5, 10, 15, 25, and 30 mm. I did not conduct the measurement at one-fourth of the axial FOV as recommended in NEMA NU-4 protocol since I have only one detector block in axial direction. Acquired data was subject to post-processing to convert it into proper list mode data using a custom-built software tool (*32*) with the energy window set to 350 – 650 keV. Four-layer DOI correction was applied by using MLE-based positioning as described earlier. List mode data was reconstructed using 3D ordered-subset estimation maximization (OSEM) reconstruction with and without DOI information. The spatial resolution of the cDOI prototype system was reported with FWHM and full-width at tenth-maximum (FWTM) values of radial and tangential profiles.

3.2.5. Phantom and animal imaging studies

Phantom study was performed using a hot rod phantom with various diameters, 1.0, 1.1, 1.2, 1.3, 1.4, and 1.5 mm respectively. The phantom was filled with 55.5 MBq ^{64}Cu positron emitting source ($T_{1/2}$=12.701 hr, λ_{e+}=17.86%), and it was placed at the center and 1.5 cm off from the center to see the imaging performance and the impact of DOI correction capability. One-hr imaging data set was acquired using our prototype system.

The animal study was approved by the Institutional Animal Care and Use Committee at Seoul National University. Two 8-week-old BALB/c mouse (25g and 27g respectively) were anesthetized by continuous administration of isoflurane mixed with oxygen. ^{18}F-FDG with activity of 45 MBq was injected to each mouse through the tail vein. After thirty minutes of uptake time, 12-min PET data set was acquired. X-ray computed tomography image was acquired before PET scan using GE eXplore VISTA PET/CT scanner.

For normalization correction, 2.96 MBq ^{68}Ge annulus source (PET-7.3A5.8; Sanders Medical Products Inc., TN, USA) which covers whole FOV was used and data were acquired for several hours to attain sufficient counts for direct normalization. No random, attenuation, and scatter correction was applied. The phantom and animal data were also reconstructed with 3D list mode OSEM with and without DOI information. An isotropic Gaussian filter with a 0.8-mm FWHM was applied to those reconstructed images. In case of hot rod phantom, 12 axial slices were summed to acquire sufficient counts.

3.3. Results

3.3.1. Detector performance

Performances of two DOI PET detectors is summarized in **Table 3-2** in terms of peak-to-valley ratio representing flood histogram quality, energy resolution, and MLE-based positioning accuracies. In this table, DOI positioning accuracies obtained using two different methods for estimating DOI (simultaneous and sequential estimations of crystal position and depth) were compared for all 324 crystals and only the crystals at left and right edges. **Figure 3-2** shows flood histogram and 2D map of positioning accuracies which is averaged over four depths.

As **Figure 3-2(a)** and **Table 3-2** shows, cDOI detectors showed good crystal identification except for the crystals at left and right edges. The blurring of edge crystals is due to our reflector configuration: crystal positions shift toward the center when events occur far from the detector. I solved this issue by applying MLE-based positioning which estimates the crystal and depth position simultaneously. By applying the simultaneous crystal and depth position estimation, described as Method 1 in **Table 3-2**, I acquired higher positioning accuracy especially at the edge crystals. Improvement in positioning accuracy can be more clearly seen in **Figure 3-2(b)** and **Figure 3-2(c)**. The cDOI detectors showed reasonably good energy resolution. By using MLE-based positioning method, interaction positions were successfully estimated to proper 324 crystal and 4 depth positions as described in **Table 3-2** (71.80% and 72.30% accuracy).

When converting positioning accuracy into DOI resolution in millimeter unit, it turned out to be 4.28 mm and 4.24 mm in average for each detector, while the best DOI resolution acquired was 3.53 mm and 3.40 mm, respectively.

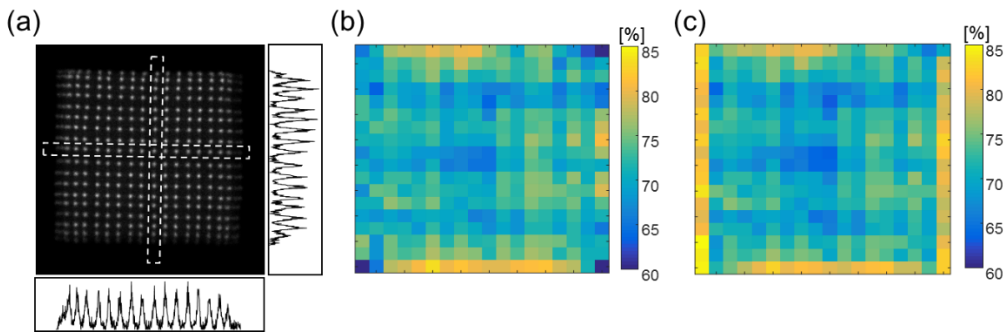

Figure 3-2 Performance of representative cDOI PET detector. (a) Flood histogram, (b) 2D map of the MLE-based DOI positioning accuracies obtained using only depth position estimation (Method 2), and (c) 2D map of the MLE-based DOI positioning accuracies determined using simultaneous crystal and depth position estimation (Method 1).

Table 3-2 DOI PET detector performances averaged over all 324 crystals.

			Block 1	**Block 2**
Peak-to-valley ratio			2.82	3.09
Energy resolution [%]			14.30 ± 1.43	18.95 ± 2.93
DOI Positioning accuracy [%]	**Method 1***	**All**	71.80 ± 4.33	72.31 ± 4.48
		Edges	73.63 ± 6.40	75.26 ± 5.73
	Method 2†	**All**	71.26 ± 4.25	71.56 ± 4.28
		Edges	68.98 ± 6.01	69.60 ± 5.75
DOI resolution [mm]			4.28 ± 0.32 (min: 3.53, max: 5.54)	4.24 ± 0.28 (min: 3.40, max: 5.06)

* Method 1: Simultaneous estimation of crystal position and depth
† Method 2: Estimation of only the depth after identifying crystal position on flood histogram

3.3.2. Spatial resolution of prototype system

I measured spatial resolution based on NEMA protocol to investigate the impact of DOI correction on the system spatial resolution. The transverse spatial resolutions in radial and tangential directions with and without DOI correction were reported in FWHM values as summarized in **Table 3-3**. **Figure 3-3** shows radial and tangential resolutions with and without DOI correction in FWHM and FWTM values. In our prototype PET system, sub-mm spatial resolution was achievable at the center of FOV. By applying MLE-based DOI correction with the accuracy of 71.80% and 72.31%, radial spatial resolution improved especially at peripheral regions (maximum 36.92% improvement). Moreover, uniform resolution was achievable within 5 cm FOV, which is enough for small animal imaging. Not only the resolution at radial direction, tangential resolution also improved after DOI correction was applied.

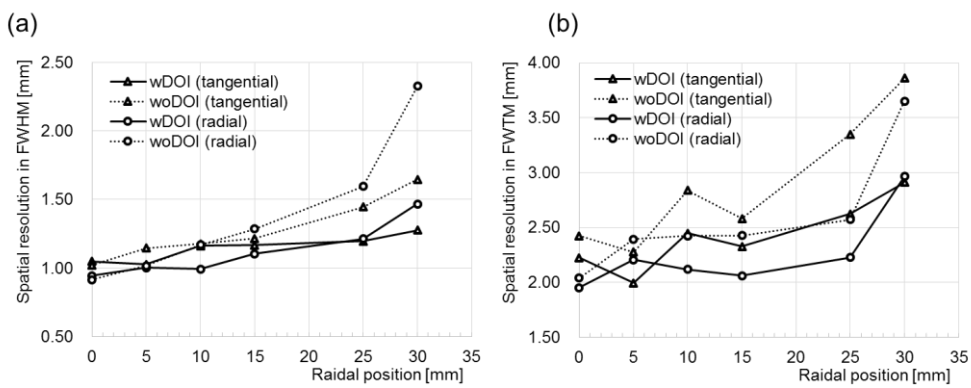

Figure 3-3 Spatial resolution of the prototype cDOI PET system measured using a ^{22}Na point source along the radial position; is reported in (a) FWHM and (b) FWTM.

Table 3-3 Spatial resolution in FWHM with and without DOI correction.

Radial position [mm]	w/ DOI correction		w/o DOI correction		Improvement [%]	
	Radial	Tangential	Radial	Tangential	Radial	Tangential
0	0.94	1.05	0.92	1.02	-3.13	-2.62
5	1.00	1.03	1.02	1.15	1.41	10.31
10	0.99	1.16	1.17	1.18	15.11	1.26
15	1.10	1.17	1.28	1.21	14.07	3.96
25	1.21	1.20	1.60	1.45	23.99	17.32
30	1.47	1.28	2.32	1.65	36.92	22.50

3.3.3. Phantom and animal imaging study

Figure 3-4 shows the reconstruction image of hot rod phantom acquired **(a)** at the center of FOV without and with DOI correction and **(b)** at 1.5 cm off center of FOV without and with DOI correction. In both cases, image resolution and resolution uniformity along FOV improved after applying DOI correction, and no significant artifact was seen in both images. In case of **Figure 3-4(a)** hot rod with size of 1.2 mm was clearly resolvable after DOI correction and even 1.1 mm hot rod was resolvable. The phantom image acquired at off-center position (**Figure 3-4(b)**) also shows that our prototype DOI PET system provides better spatial resolution over entire imaging FOV after DOI correction.

Figure 3-5 shows the reconstruction images of mouse acquired **(a)** without DOI correction, and **(b)** with DOI correction. By using our prototype system, myocardial uptake was clearly seen in mouse after DOI correction. Even our prototype system was demonstrated by just two detector module which is not

easy to acquire sufficient counts, DOI correction using our DOI encoding method was revealed to be effective.

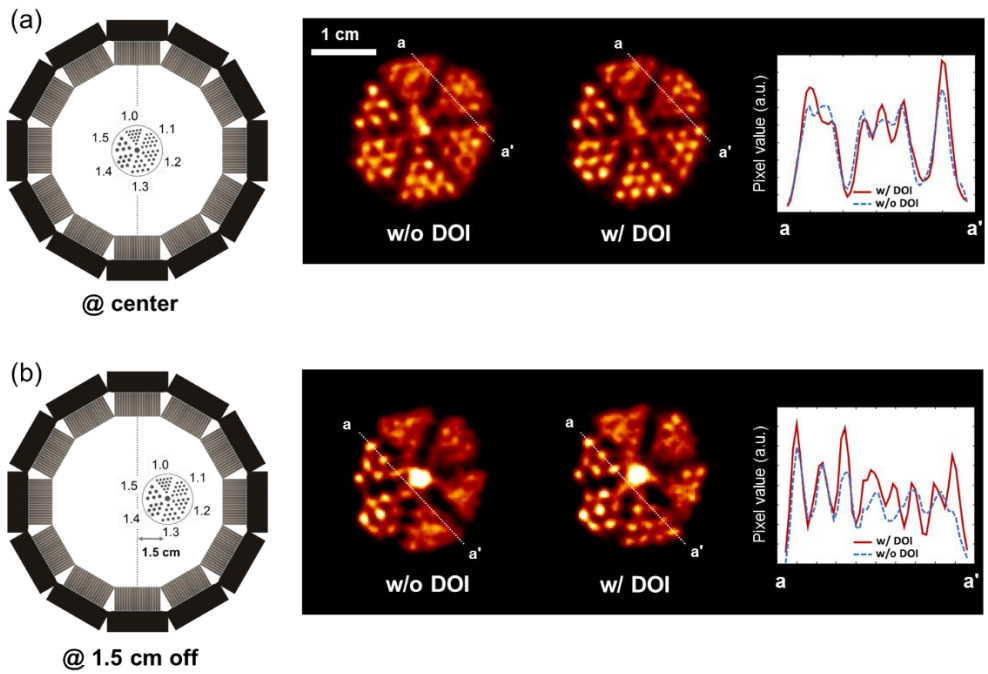

Figure 3-4 Hot-rod phantom images acquired using the prototype cDOI PET system. The hot-rod phantom was filled with ^{64}Cu and data were acquired for 60 min. Images obtained without and with the DOI correction (a) at the center of the FOV and (b) at 1.5 cm from the center of the FOV.

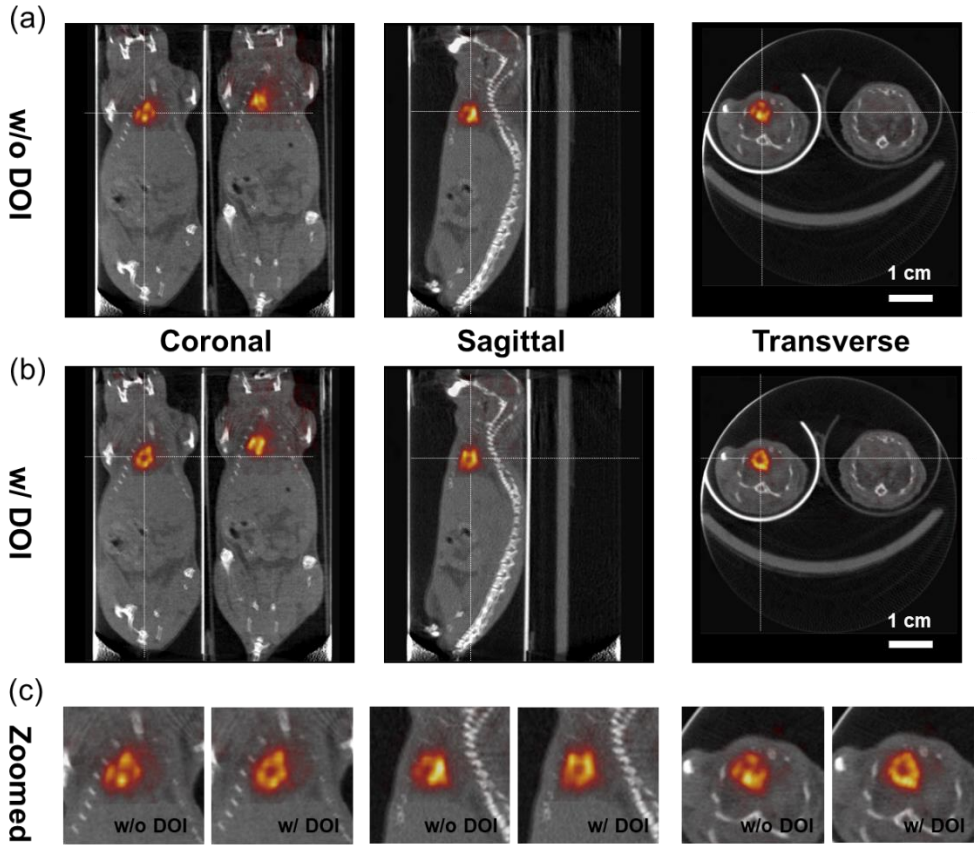

Figure 3-5 PET/CT images of BALB/c mice acquired after injection of ^{18}F-FDG acquired for 12 min. Images obtained (a) without the DOI correction and (b) with the DOI correction. (c) Zoomed myocardial regions for the left mouse.

3.4 Discussion

In this study, an animal-dedicated proof-of-concept DOI PET system was developed using a pair of detector and two rotation stages. The DOI detector pair showed good intrinsic performances. I obtained the depth positioning accuracies of 71.80 and 72.3% using MLE-based positioning method with four-step depth calibration data. I could not well discriminate the merged crystals at edges using conventional crystal clustering method that is based on the flood histogram generated by center of mass calculation, providing wrong crystal and depth information (**Figure 3-2(a), (b)**). Depth-dependent flood histogram generation is one of the possible solutions for more accurate crystal identification (*24*). The MLE-based positioning which estimates crystal and depth position simultaneously is another approach to classify the merged crystals. By comparing positioning accuracies in merged crystal at edges as reported in **Table 3-2**, MLE-based 3D positioning turned out to be successful in this study.

Regarding the positioning accuracies, simultaneous 3D position estimation was turned out to have higher positioning accuracy than sequential estimation. Based on MLE positioning, I obtained approximately 4 mm of average DOI resolution which enables four-step DOI correction in 15-mm long LYSO crystal. The MLE-based positioning demands relatively long computation time and large memory consumption. If this algorithm is applied to the next-generation full-ring system, a hardware/firmware implementation of this algorithm will be necessary for real-time position estimation.

Based on the four-step DOI correction, I observed considerable improvements in spatial resolution and resolution uniformity especially at the peripheral FOV. Sub-mm spatial resolution was observed within 2 cm FOV, and uniform resolution was achieved within the 5 cm FOV after DOI correction. The impact of DOI correction was also obvious in the phantom and animal imaging studies. After DOI correction, resolution uniformity increased and hot lesions up to 1.1 mm size was well resolved. I expect to have better image resolution and contrast with additional scatter, attenuation and random corrections.

There were several limitations in the demonstration of a ring-like PET system using a pair of detector. Since I used two motorized rotation stages, there might exist artifacts arisen from the detector misalignment and center-of-rotation error. The impact of detector misalignment is greater in two detector system than a full-ring system because LOR mis-positioning caused by the misalignment arises in every angle. These systematic errors might lead to spatial resolution and image contrast degradation. In addition, it is difficult to acquire sufficiently large number of counts in the PET studies using the radioisotopes with short half-life (e.g. ^{18}F with 2 hour) and the PET detector pair. Hence I expect to have better image quality in our next-generation full-ring system.

Chapter 4. Inter-crystal event identification

4.1. Background

ICS events cause mis-positioning of gamma interaction position resulting in false LORs, and false LORs lead to degradation in image resolution and contrast. ICS is a common phenomenon in PET detectors since the energy range used in PET has a large cross section in Compton scattering. Especially, for the high-resolution application with the narrower crystal element, the occurrence of ICS increases (*33*). The occurrence of ICS depends on the scintillation material and detector geometry and about 27% of events undergo ICS in a PET detector (e.g. detector with 10×10 array of 3×3×20 mm^3 crystal element). Hence, by identifying the interaction position and deposited energy of the ICS event and recovering them into the first interaction position, we can minimize resolution degradation and maximize system sensitivity.

However, it is very challenging to discriminate ICS events within the PET detector, because most of the current PET detectors use the light sharing between scintillation crystals and photo sensor pixels and multiplexed signal readout (*34*). Up to now, using the 1-to-1 coupling between a crystal and a photo sensor pixel with individual signal readout scheme is one feasible way for the ICS event identification (*34, 35*). However, this approach has a limitation in achieving good spatial resolution because it is technically hard to produce multi-pixel photo sensors with sufficiently small pixel sizes for the high resolution applications.

The image reconstruction with point spread function (PSF) modeling technique can be another alternative solution to mitigate resolution degradation by including ICS in modeling (*36, 37*). However, this approach requires a large data sets containing PSF responses of a system and a long reconstruction time.

In this study, I propose a new method to classify and identify ICS events. I modeled the detector observation as a linear problem, and by solving a linear problem ICS events were identified. The proposed method was applicable in the light sharing design with multiplexing readout scheme, which was not feasible with existing technologies. Here, I investigated the proposed ICS identification method by Monte Carlo simulation and experimental studies. Based on the new ICS identification method, ICS events were recovered into the first interaction position to see the impact of ICS correction.

4.2. Materials and methods

4.2.1. ICS event identification

4.2.1.1. Proposed algorithm

The proposed ICS event identification algorithm is based on a simple idea by modeling the detector observation and event characteristics as a linear problem. When I suppose a 511-keV gamma ray fully deposits its energy at a single crystal, the observation vector, $\boldsymbol{y}$, can be expressed as below **Equation 4-1** which is consisted of m detector (photo sensor) responses.

$$\boldsymbol{y} = [y_1, \dots, y_m]^{\mathbf{T}} \qquad \textbf{(4-1)}$$

Consider that an ICS event occurred at i^{th} and j^{th} crystals by depositing energies of E_i and E_j ($E_{\text{total}} = E_i + E_j$). Then the observation $\boldsymbol{y}$ of an ICS event can be expressed as the sum of independent observations of $\boldsymbol{y}_{\text{i}}$ and $\boldsymbol{y}_{\text{j}}$ multiplied with the corresponding energy ratios (**Equation 4-2**).

$$\boldsymbol{y} = \boldsymbol{y_i} \times \frac{E_i}{E_{total}} + \boldsymbol{y_j} \times \frac{E_j}{E_{total}} \qquad \textbf{(4-2)}$$

The observation $\boldsymbol{y}$ of a single ICS event can be simply converted into a matrix formation of

$$\boldsymbol{y} = \boldsymbol{A}\boldsymbol{x};\ \begin{bmatrix} y_1 \\ \vdots \\ y_m \end{bmatrix} = \begin{bmatrix} a_{1,1} & \cdots & a_{1,n} \\ \vdots & \ddots & \vdots \\ a_{m,1} & \cdots & a_{m,n} \end{bmatrix} \times \begin{bmatrix} x_1 \\ \vdots \\ x_n \end{bmatrix} \qquad \textbf{(4-3)}$$

, where $\boldsymbol{y}$ is a [m×1] vector of ICS event observations, $\boldsymbol{A}$ is a [m×n] matrix of characteristic m detector responses for n crystals, and $\boldsymbol{x}$ is a [n×1] vector of energy ratios for n crystals. The vector $\boldsymbol{y}$ is a known value which is the observation of a single gamma event, and matrix $\boldsymbol{A}$ is also a known value that can be generated from typical detector data sets by calculating mean detector

responses that underwent PE events for each crystal position. Consequently, finding the vector $\boldsymbol{x}$, I can identify ICS event positions and corresponding deposited energies.

To find vector $\boldsymbol{x}$, I suggest and compared three different ICS identification methods. Interacted crystal positions and deposited energies of each events were identified.

1) Method 1: maximum peak detection

$$\max(\boldsymbol{y})$$

2) Method 2: pseudo inverse matrix calculation

$$\boldsymbol{x} = (\boldsymbol{A}^{\mathrm{T}}\boldsymbol{A}^{-1})\,\boldsymbol{A}^{\mathrm{T}}\boldsymbol{y}$$

3) Method 3: convex constrained optimization

$$\arg\min_{\boldsymbol{x}} \|\boldsymbol{y} - \boldsymbol{A}\boldsymbol{x}\|_2$$

$$\text{subject to} \quad \boldsymbol{x} > 0,$$

$$\sum \boldsymbol{x} = 1$$

Method 1 is a typical approach that is used in 1-to-1 coupling detector with individual signal readout and this method was tested, and Method 2 and 3 are the proposed ICS identification methods. To solve the above linear problem, I simply calculate a pseudo inverse matrix as Method 2. However, a pseudo inverse matrix can have negative entries. Hence, Method 3 was proposed to solve the linear problem with given constraints as the above equation, and convex constrained optimization was used to find the solution. Matlab-based CVX program (*38*) was used.

4.2.1.2. Event classification and identification

The list mode events were classified into two event types of Photo Electric (PE) absorption and ICS by using three different identification methods as explained in section **4.2.1.1**. Each event was classified as following criteria, while the constant *c* was determined based on the simulation.

1) PE events: $\frac{\max(\boldsymbol{x})}{\text{second } \max(\boldsymbol{x})} > c$,

2) ICS events: $\frac{\max(\boldsymbol{x})}{\text{second } \max(\boldsymbol{x})} \leq c$

Classified ICS events were identified into interacted positions and energies by using indices and values of energy ratio vector ($\boldsymbol{x}$). Consider a case that ICS event occurred only once, *indices* of two maximum values in a vector $\boldsymbol{x}$ were determined as interacted crystal positions and *values* of vector $\boldsymbol{x}$ was determined as deposited energy ratios. **Figure 4-1** shows the energy ratio vector ($\boldsymbol{x}$) of typical PE and ICS events that is acquired by convex optimization method.

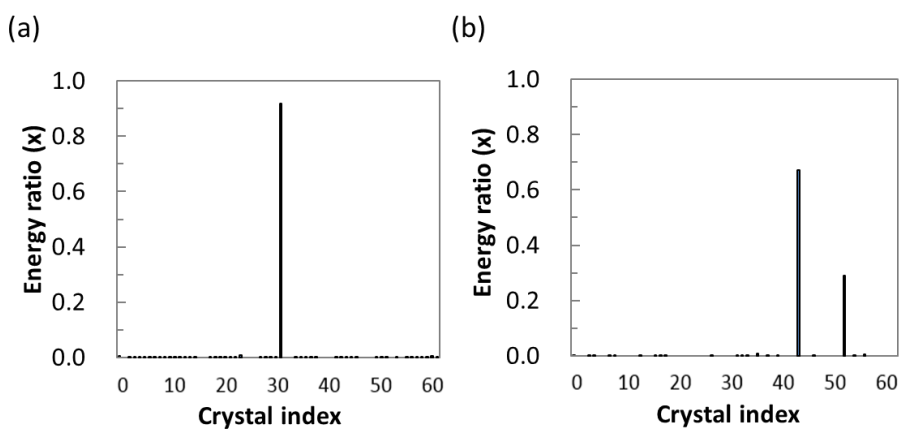

Figure 4-1 Energy ratio vectors for the representative (a) PE events and (b) ICS events.

As the performance evaluation, *identification rate* was calculated, which is the number of correctly identified events into the first interaction position over the total number of events. Also, energy linearity and correlation were evaluated by conducting a linear fitting of the true energy values and estimated energies.

4.2.2. Monte Carlo simulation study

To evaluate the proposed methods, a simulation study was conducted using GATE v.7.0 Monte Carlo simulation toolkit (*28*) with optical photon tracking. The photo sensor was simulated to have the same geometry as a commercial dSiPM, which is consisted of 8×8 pixels (3.2×3.8775 mm^2). The simulated dSiPM was coupled with arrays of polished LSO (Lu_2SiO_5; d = 7.5g cm^{-3}; refractive index 1.82; light yield 26000 photons MeV^{-1}) crystals. LSO crystals were wrapped with reflectors with the reflectivity of 98% and all the gaps in between crystals were set to be air. The photo sensor and crystal array were optically coupled with 0.1 mm thick optical adhesive ($C_1H_1O_1$; d = 1.0 g cm^{-3}; refractive index 1.465). Three detector configurations with different crystal-to-sensor coupling ratios were used as following **Table 4-1** to simulate the 1-to-1 coupling and two light sharing designs.

Table 4-1 Specifications of simulated detector configurations

Crystal-to-sensor coupling ratio	Crystal size [mm^3]	Crystal array size
1:1	3×3×20	8×8
1.25:1	3×3×20	10×10
1.5:1	2.5×2.5×20	12×12

All crystal surfaces and medium boundaries were simulated using the 'ground model' based on the UNIFIED model (*39*). The detector was uniformly irradiated using a 511-keV gamma point source and 8×8 detector responses were acquired. Moreover, three representative signal readout schemes were applied on the simulated 8×8 detector responses to investigate the effect of signal multiplexing on the proposed algorithm. The detector individual readout (1:1 signal multiplexing), row-and-column sum (RC sum) readout (4:1 signal multiplexing), and four corner readout (16:1 signal multiplexing) schemes were applied. Identification rate and energy linearity performances were evaluated by using three identification methods based on the simulation study.

4.2.3. ICS event recovery scheme

Choosing the first interaction position among two or more interacted positions of an ICS event is important as well as event identification. Techniques to choose the first interaction position have been previously investigated by several groups, such as choosing the interaction position with the maximum energy deposition (*33, 40*) or choosing the interaction position that satisfies Compton kinematics (*35*). In this study, I used the proportional method (*41*), which distributes multiple coincidence events among their possible LORs using the relative proportions of double coincidences in that corresponding LORs as the following **Equation 4-4**.

$$\mathrm{LOR}_{i-j} = D_{i-j} + \sum_{k}^{n} \left(\frac{D_{i-j}}{D_{i-j} + D_{i-k} + D_{j-k}}\right) T_{i-j-k} \qquad \textbf{(4-4)}$$

The proportional method was originally suggested for recovering inter-block scattering events in PET system level, but here I extended the method to ICS events in PET detector level. Here, $\mathrm{LOR}_{i\text{-}j}$ represents the final number of counts including PE and ICS events along the LOR connecting the interacted crystal pair i and j. $\mathrm{D}_{i\text{-}j}$, $\mathrm{D}_{i\text{-}k}$, $\mathrm{D}_{j\text{-}k}$ represents the number of coincidences that underwent PE along interaction positions $i - j$, $i - k$, and $j - k$. $\mathrm{T}_{i\text{-}j\text{-}k}$ is the number of coincidences that underwent ICS at positions i, j, and k. And the upper equation is known as a maximum-likelihood estimate for the mean number of counts along $\mathrm{LOR}_{i\text{-}j}$.

The ICS recovery schemes were initially investigated by using simulation. ICS events were identified with the convex optimization method and they were recovered by using the proportional method. The ICS recovered results were compared to the true value and the maximum energy deposition method.

4.2.4. Experimental study

Experimental studies were conducted to validate the proposed methods. The 1-to-1 coupling and light sharing detectors were constructed using Philips dSiPMs coupled with 3×3×20 mm^3 LGSO ($\mathrm{Lu}_{1.9}\mathrm{Gd}_{0.1}\mathrm{SiO}_5$:Ce; Hitachi Chemical, Tokyo, Japan) crystal arrays. For the 1-to-1 coupling design, 8×8 crystals were

individually coupled with 8×8 sensor pixels. For the light sharing design, a 10×10 crystal array was coupled with 8×8 sensor pixels. Each crystal was wrapped with ESR except for the one face that was optically coupled with the dSiPM. The 8×8 detector responses were recorded individually by PDPC Technical Evaluation Kit. Post-processing was applied to demonstrate the 4:1 RC sum signal multiplexing. Sensor configurations of the dSiPM were set to trigger level 4, validation level 8, integration length 165 ns, full neighbor logic, and 40 ns coincidence window.

Intrinsic spatial resolutions of a detector pair were measured by moving a ^{22}Na point source in the axial direction with a step size of 0.5 mm from the center to the edge of the detector pair. The counts of opposite crystal pair along positions were acquired and represented as a count profile for both 1-to-1 and light sharing detectors. Count profiles of four crystals were acquired with the energy window of 350 – 650 keV. The detector pair was located each other at the distance of 13 cm. The experimental set up was placed inside the temperature control box set to 15 ℃.

Three ICS identification methods were applied to experimental data for event classification and identification. The matrix $\boldsymbol{A}$ was generated based on the flood histogram of a typical detector data set with uniform irradiation; here, ICS events were rejected by applying Anger mask (*26*). Events were classified into PE and ICS events, and the interacted positions and energy ratios were identified using three identification methods. The identified ICS events were recovered into

the first interaction position using the proportional method. Gaussian fitting was applied to the ICS event recovered count profiles of four opposing crystal pairs, and FWHMs and FWTMs were calculated. Intrinsic resolutions averaged over four crystal positions were reported in FWHMs and FWTMs.

4.3. Results

4.3.1. Simulation results

4.3.1.1 1-to-1 coupling design

Performances of ICS identification methods, the identification rate and energy linearity, were investigated for the 1-to-1 coupling design based on the simulation study. The good identification performances represent the accurate ICS event recovery into the first interaction position. Three different readout methods were tested and three different identification methods were applied as shown in **Table 4-2**. With the individual signal readout (1:1 signal multiplexing), three identification methods showed the highest identification rates. Among them, the proposed pseudo inverse and convex optimization methods showed better identification rates compared to max peak detection method which is a typical approach to identify ICS events. When I consider events with more than one ICS occurrence, higher identification rates were observed that almost reached 1. After 4:1 signal multiplexing from 8×8 detector signals I lose accuracy in light distribution information, and the identification rate degraded for all cases. However, the convex optimization method still showed reasonably good identification rate of 0.72. In case of 16:1 signal multiplexing, ICS events could not be identified at all.

As energy estimation performances, the estimated deposited energies of ICS events were fitted with the true energies as shown in **Figure 4-2**. The 1:1 signal multiplexing case showed good linearity and correlations with the true energy

for the three identification methods. After 4:1 signal multiplexing, the linearity and correlation degraded in max peak detection and pseudo inverse method, but convex optimization method still showed good and consistent linear relationship. The 16:1 multiplexing case was not applicable at all.

Table 4-2 ICS identification performances of the simulated 1-to-1 coupling detector.

Signal multiplexing ratio	**Identification method**	**ICS identification rate (ICS # = 1)**	**ICS identification rate (ICS # ≥ 1)**
1:1	Max peak detection	0.86	0.93
	Pseudo inverse	0.93	0.98
	Convex optimization	0.93	0.98
4:1	Max peak detection	0.60	0.61
	Pseudo inverse	0.65	0.70
	Convex optimization	0.72	0.81
16:1	Max peak detection	Not applicable	Not applicable
	Pseudo inverse	0.02	0.03
	Convex optimization	0.02	0.03

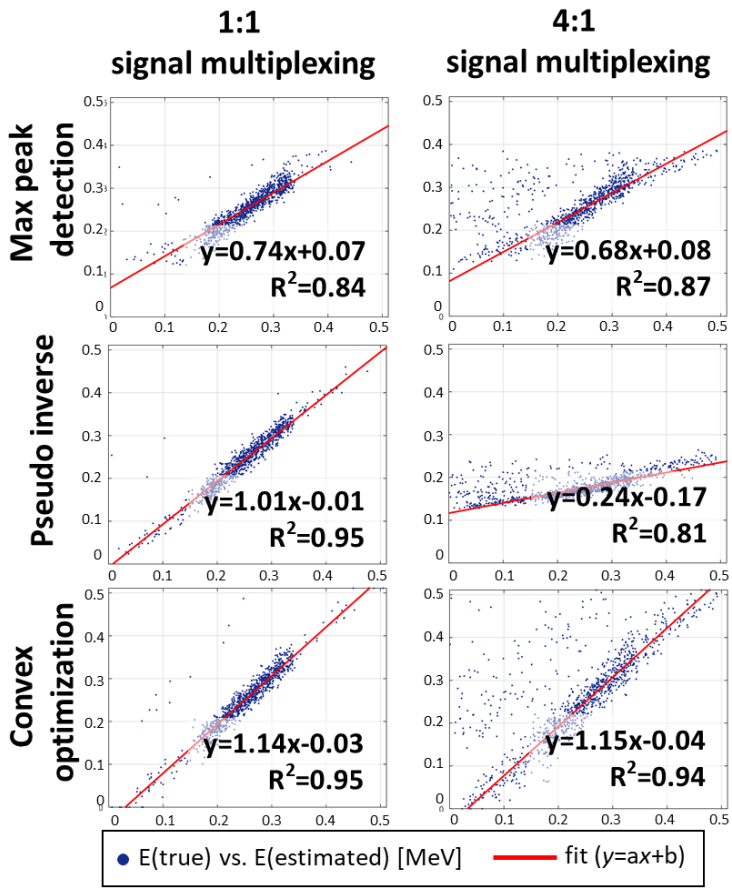

Figure 4-2 Energy estimation performances for the 1-to-1 coupling design detector. Three different identification methods were applied for the two different signal multiplexing methods.

4.3.1.2 Light sharing design

Table 4-3 shows ICS event identification performances of two light sharing detectors with different crystal-to-coupling ratios. The two proposed identification methods were applied since the max peak detection method was not applicable in light sharing detectors. For the light sharing detector with 1.25:1 crystal-to-sensor coupling ratio without signal multiplexing, I achieved good ICS identification rate of 0.87 with the convex optimization method. With 4:1 signal multiplexing, identification rate degraded. For the light sharing detector with higher crystal-to-sensor coupling ratio of 1.5:1, the ICS identification rate degraded compared to lower coupling ratio. Still, with 1:1 signal multiplexing, I achieved reasonably good ICS identification of 0.76 with the convex optimization method. For the both light sharing detectors, the pseudo inverse method did not show good identification performance.

As energy estimation performances of light sharing detectors were shown in **Figure 4-3**. For all cases, the pseudo inverse method showed poor energy linearity and correlations. On the other hand, the convex optimization method showed consistent energy linearity and high correlations even though there were slight degradations with higher crystal-to-sensor coupling ratio.

Table 4-3 ICS identification performances of the simulated light sharing detectors.

Crystal-to-sensor coupling ratio	Signal multiplexing ratio	Identification method	ICS identification rate (ICS # = 1)	ICS identification rate (ICS # ≥ 1)
1.25:1	1:1	Pseudo inverse	0.67	0.80
		Convex optimization	0.87	0.94
	4:1	Pseudo inverse	0.53	0.62
		Convex optimization	0.65	0.73
1.5:1	1:1	Pseudo inverse	0.56	0.67
		Convex optimization	0.76	0.83
	4:1	Pseudo inverse	0.48	0.57
		Convex optimization	0.56	0.64

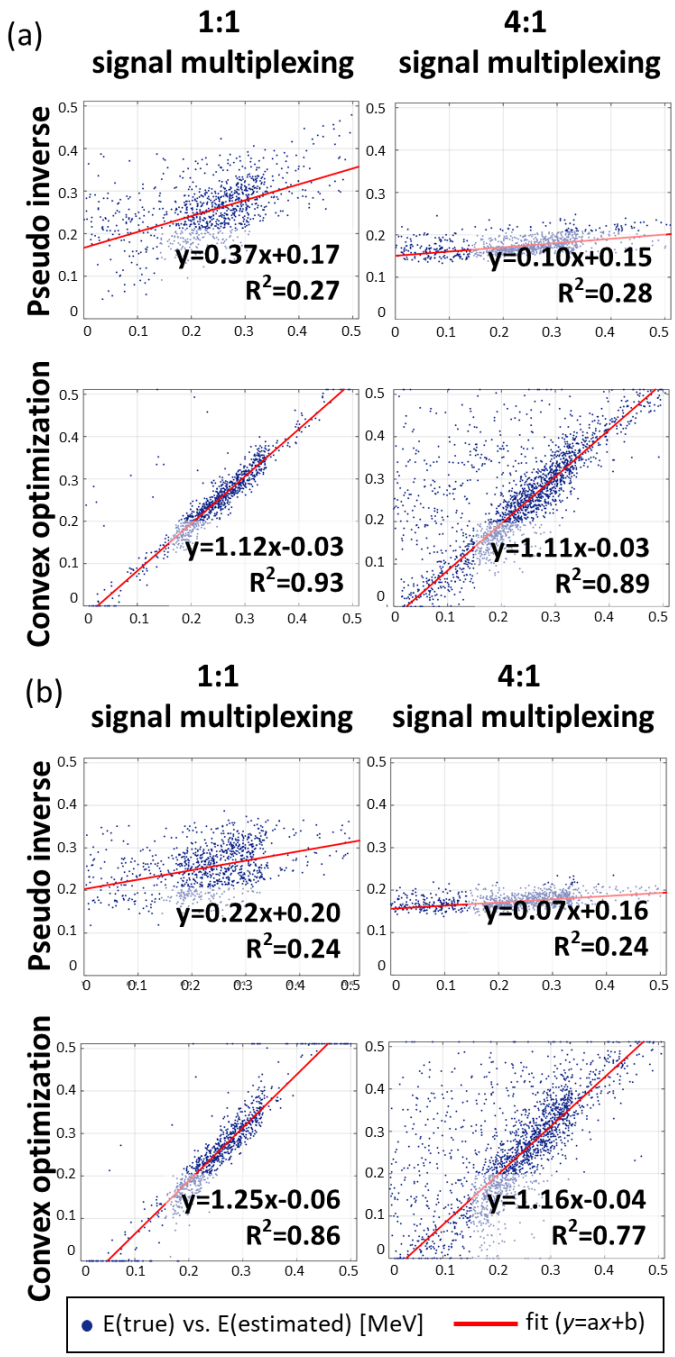

Figure 4-3 Energy estimation performances for the light sharing design detectors. Two different identification methods were applied for the two different signal multiplexing methods.

4.3.1.3 ICS event recovery

ICS recovery schemes were implemented on the simulation data and compared with true values. **Figure 4-4** shows the count profile with and without ICS recovery for 1-to-1 and light sharing detectors. For both detector designs, the count profiles were sharpened after ICS recovery by recovering mis-positioned LORs into the true LORs. Proportional method showed the better recovery performances compared to maximum energy deposition method regardless of ICS identification methods. However, the existing ICS recovery techniques could not fully recover events into the true interaction positions as shown in **Figure 4-4**. The proportional method was used to recover ICS events in this study.

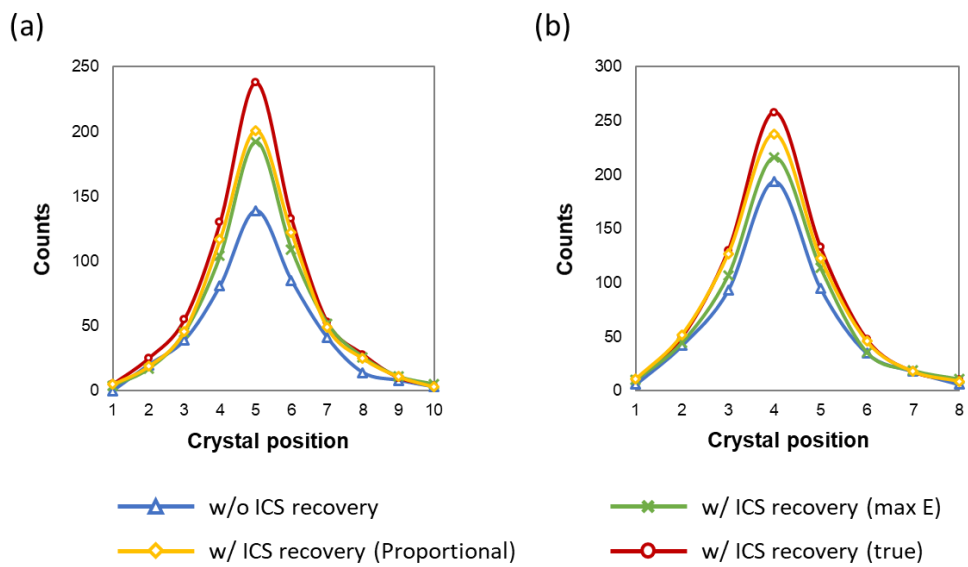

Figure 4-4 ICS event recovered results using several recovery methods for the (a) 1-to-1 coupling and (b) light sharing detectors.

4.3.2. Experimental results

4.3.2.1 1-to-1 coupling design

As an experimental validation, intrinsic spatial resolution was measured for a detector pair. Events were classified and identified using three ICS classification methods and recovered into the first interaction position. Events with and without ICS recovery were shown in normalized count profiles as **Figure 4-5**. Two signal multiplexing schemes which are 1:1 and 4:1 signal multiplexing schemes were investigated. Intrinsic resolutions averaged over four crystal positions were reported in **Table 4-4**.

As shown in the **Figure 4-5**, I observed sharpened count profile with increased intensities after ICS recovery by using the proportional method. When I recovered ICS events, which were identified with the proposed methods, I observed about a 1.5-fold increase in count profile intensity compared to the case without ICS recovery. The max peak detection method, which is the typical approach for ICS event identification, showed an only 1.14-fold increase in the count profile intensity. Especially for the bottom parts of the count profiles, profiles were narrowed after ICS recovery using the proposed ICS event identification. Average intrinsic resolutions in FWHM and FWTM for 1-to-1 detector with 1:1 signal multiplexing were 1.95 and 3.56 mm without ICS recovery, and improved to 1.72 and 3.14 mm after recovering ICS events identified by the convex optimization method. By recovering ICS events, I get closer to the ideal intrinsic resolution of 1.5 mm.

When detector signals were multiplexed with 4:1 ratio, the increase in count profile intensity was not so significant compared to 1:1 signal multiplexing. However, still, the proposed methods showed improvement in intrinsic resolutions. The average intrinsic resolutions in FWHM and FWTM were improved to 1.78 and 3.24 mm with ICS identification using the convex optimization method.

Table 4-4 Intrinsic resolutions of the 1-to-1 coupling detector.

Signal multiplexing ratio	**Event identification method**	**FWHM [mm]**	**FWTM [mm]**
1:1	Not applied	1.95	3.56
	Max peak detection	1.80	3.29
	Pseudo inverse	1.72	3.13
	Convex optimization	1.72	3.14
4:1	Not applied	1.95	3.56
	Max peak detection	1.82	3.32
	Pseudo inverse	1.77	3.22
	Convex optimization	1.78	3.24

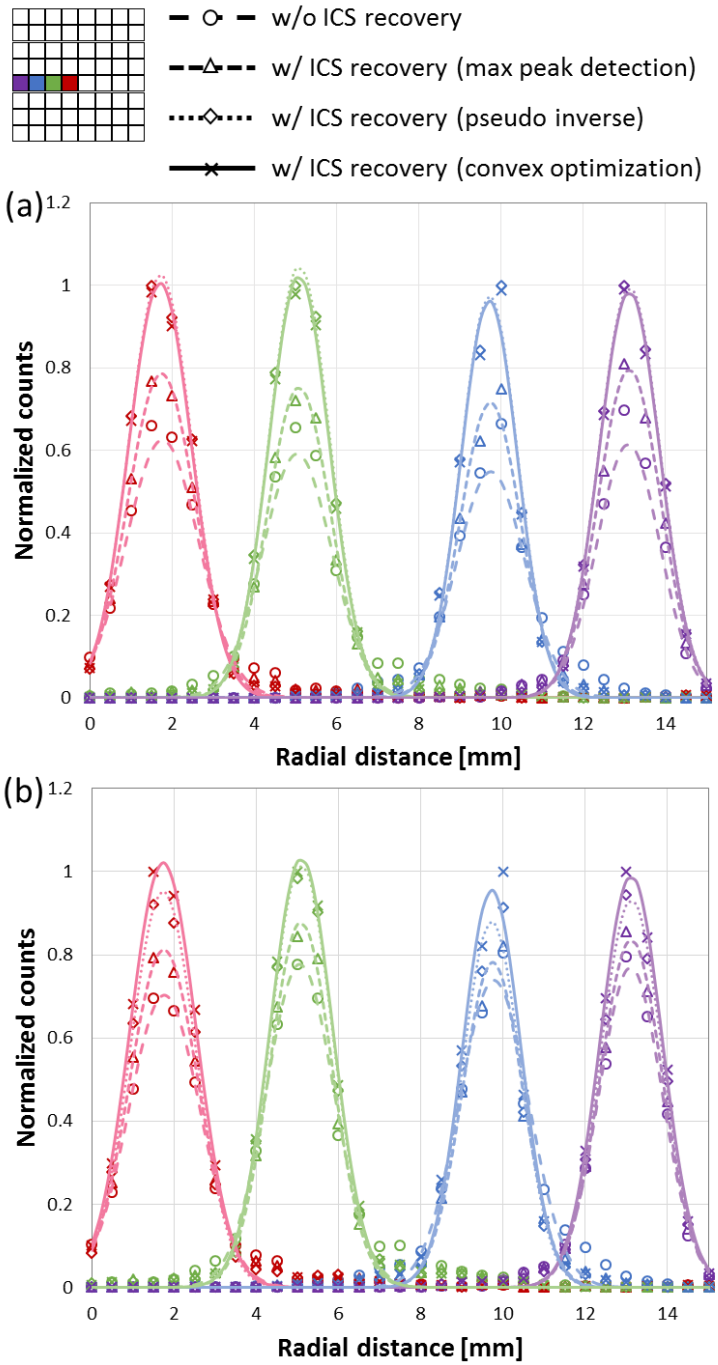

Figure 4-5 Intrinsic resolution profiles of 1-to-1 coupling detector in case of (a) individual readout and (b) row-and-column sum readout.

4.3.2.2 Light sharing design

The light sharing detector was also used for experimental validation with the same procedure as the 1-to-1 coupling detector. Since max peak detection method was not applicable, the pseudo inverse and convex optimization methods were used for ICS event identification. Events with and without ICS recovery were shown in normalized count profiles as **Figure 4-6**. Intrinsic resolutions averaged over four crystal positions were reported in **Table 4-5**.

In **Figure 4-6(a)**, which is the case of 1:1 signal multiplexing, I observed a 1.44-fold increase in count profile intensity after recovering ICS events that are identified using convex optimization method. Average intrinsic resolutions in FWHM and FWTM for light sharing detector with 1:1 signal multiplexing were 2.25 and 4.10 mm without ICS recovery, and improved to 1.83 and 3.34 mm after recovering ICS events identified by the convex optimization method. Intrinsic resolutions were degraded compared to 1-to-1 coupling detector for all cases. However, when I recover ICS events in light sharing detector, I can achieve better intrinsic resolution than the 1-to-1 coupling detector without ICS recovery. The pseudo inverse method showed slight improvement but not so significant compared to the convex optimization method. Especially, for the blue crystal in **Figure 4-6(a)** showed almost similar profile in case of without ICS recovery and with ICS recovery (pseudo inverse), because this crystal was located near the large gap of the dSiPM pixels. However, the convex optimization method showed good results regardless of crystal positions.

When 4:1 signal multiplexing was applied, count profiles showed different tendency and showed degraded performances in the pseudo inverse method. This was mainly due to the loss in detector information after signal multiplexing leading to mis-identification of ICS events especially for the crystals located in the sensor pixel gaps. However, the convex optimization method showed robust event identification in light sharing detector with signal multiplexing; even though it showed slight degradation. The average intrinsic resolutions in FWHM and FWTM were 2.25 and 4.10 mm without ICS recovery and improved to 1.88 and 3.43 mm after recovering ICS events identified with the convex optimization method.

Table 4-5 Intrinsic resolutions of the light sharing detector

Signal multiplexing ratio	**Event identification method**	**FWHM [mm]**	**FWTM [mm]**
1:1	Not applied	2.25	4.10
	Pseudo inverse	2.06	3.75
	Convex optimization	1.83	3.34
4:1	Not applied	2.25	4.10
	Pseudo inverse	2.12	3.86
	Convex optimization	1.88	3.43

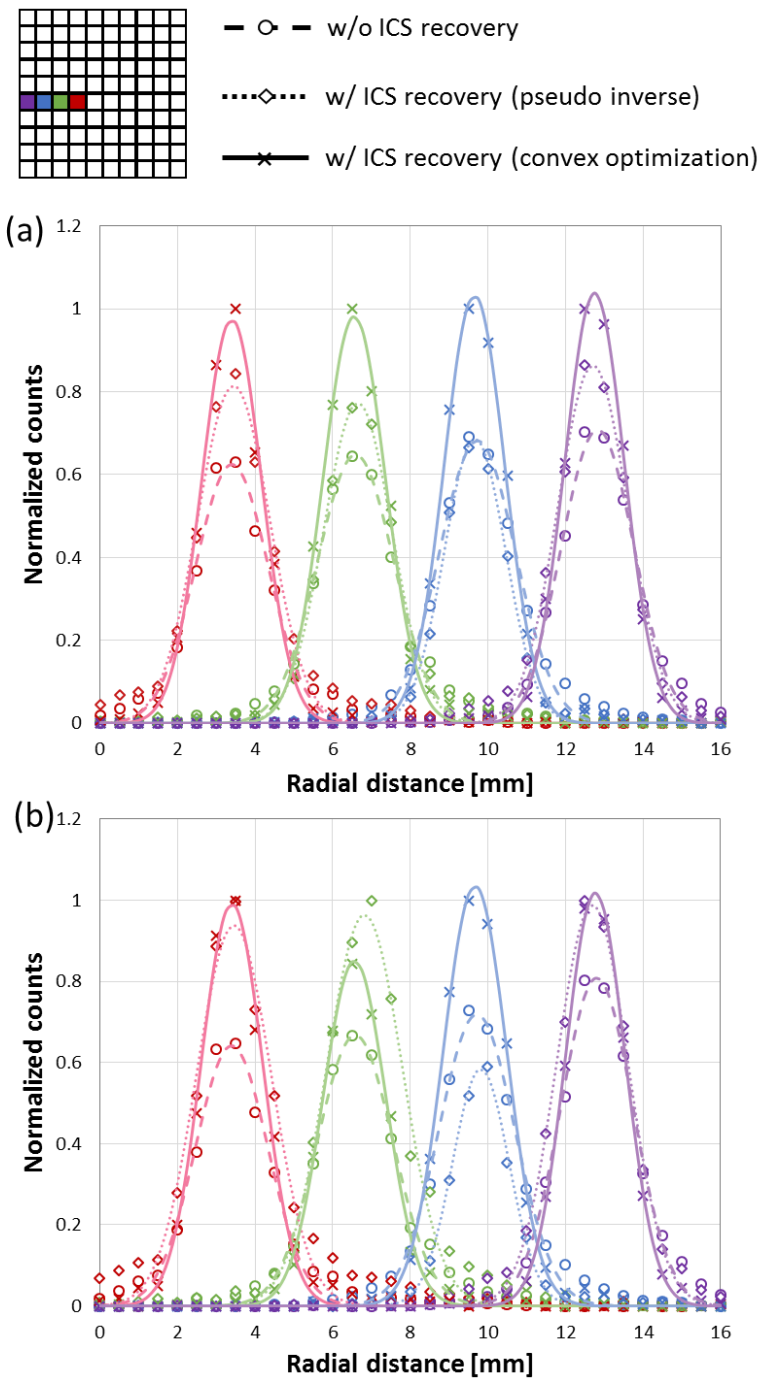

Figure 4-6 Intrinsic resolution profiles of light sharing detector in case of (a) individual readout and (b) row-and-column sum readout.

4.4. Discussion

In this study, I developed a new approach to identify ICS events in the PET detector by solving a linear problem which was modeled based on the detector observation and event characteristics. I suggested two methods to find a solution of the linear problem, the first was to calculate the pseudo inverse matrix and the second was to solve the convex constrained optimization problem. Both methods have pros and cons, the pseudo inverse method is very simple and fast but it can yield negative entries in energy ratio vector $\boldsymbol{x}$, which will lead to false estimation in identifying interacted positions and energies. The convex optimization method can give us highly accurate energy ratio vector $\boldsymbol{x}$ by giving constraints, but it requires quite long computation time. The proposed algorithm has advantages in that it has no dependency on system or detector geometry.

Based on the simulation study, I investigated performances ICS identification methods. The proposed methods showed better performance compared to the maximum peak detection approach that is typically used in 1-to-1 coupling designs. From this results, I can infer that maximum peak positions in detector responses do not represent the real interacted positions, whereas finding maximum energy deposited positions in detector led to higher event identification rate. Signal multiplexing led to imprecise detector response information, and the ICS identification performance degraded especially in case of max peak and pseudo inverse method. However, the proposed convex optimization method showed reasonably good ICS identification rate and the

consistent energy linearity even after 4:1 signal multiplexing. From this study, I found at least 4:1 signal multiplexing is required to preserve detector response information.

The proposed convex optimization method was also applicable on the light sharing detectors which is a new technology. I achieved good ICS identification rate of 0.87 with the light sharing detector consisted of 10×10 crystal array coupled with 8×8 sensor pixels. Energy linearity of the convex optimization method was consistent for the light sharing designs as the 1-to-1 coupling designs. The slope of the fitted energy curve was not 1, but this is not a big issue since it can be post-calibrated based on the simulation data. Crystal-to-sensor coupling ratio larger than 1.5:1 was challenging to identify ICS events.

As an experimental study, I performed intrinsic spatial resolution measurement for the 1-to-1 and light sharing detector. After recovering ICS events into the first interaction position using the convex optimization method, I experimentally validated intrinsic resolution is improved after ICS recovery. In the 1-to-1 coupling design, I observed resolution improvement from 1.95 mm into 1.72 mm in FWHM and 3.56 mm into 3.14 mm in FWTM. Moreover, in the light sharing design, I observed resolution improvement from 2.25 mm into 1.83 mm in FWHM and 4.10 mm into 3.34 mm in FWTM. Light sharing detector with 4:1 signal multiplexing also showed resolution improvement, even though individual signal readout showed much better results. Since the intrinsic spatial resolution is directly related to the system spatial resolution, I expect achieve

better system spatial resolution by using recovering ICS events using the convex optimization method.

Chapter 5. Conclusion

In this study, we developed two different PET detector technologies to improve PET system spatial resolution. As a first study, DOI information encoding/decoding technologies were developed and evaluated in the detector level to enhance *z*-axis positioning accuracy. By combining dSiPM technology and the proposed ML-based DOI positioning, we obtained continuous DOI information with the high DOI positioning accuracy. After several optimization processes, good DOI positioning accuracy of 63.97%±4.64% which is 4.67 mm in DOI resolution was observed; which realized five-step *z*-axis positioning for the 20-mm-long crystal.

As a subsequent study, a prototype PET system with a DOI-encoding capability was developed that is cost effective, allows easy crystal identification, and yields good energy and DOI resolutions. The developed animal-dedicated prototype system showed sub-millimeter spatial resolution at the center of FOV. By using DOI information based on the developed DOI measurement technologies with an accuracy of 71.80% and 72.31% for 15-mm-long crystal, the resolution degradation due to parallax errors were reduced. The system resolution improvement was observed after applying DOI correction in the range between minimum 1.4% up to maximum 36.92%. Moreover, the phantom and animal imaging studies showed that the proposed DOI-encoding/decoding technologies successfully improves PET image resolution and quality.

As a last study a new method to classify and identify ICS events in PET detectors was firstly proposed that is applicable in all detector configurations. By identifying ICS events, we can improve *x*- and *y*-direction positioning accuracy in PET detector. Based on the Monte Carlo simulation study, we revealed that the proposed method based on convex constrained optimization yield robust energy estimation and high ICS identification rates of 0.93 and 0.87 for 1-to-1 coupling and light sharing detectors. Experimental study showed the resolution improvement after recovering ICS event that was identified with the proposed methods. Average intrinsic resolutions in FWHM and FWTM for the 1-to-1 detector were 1.95 and 3.56 mm without ICS recovery and improved to 1.72 and 3.14 mm after ICS recovery. Average intrinsic resolutions in FWHM and FWTM for the light sharing detector were 2.25 and 4.10 mm without ICS recovery and improved to 1.83 and 3.34 mm after ICS recovery. Based on the experimental study, the proposed method showed 19.1% improvement in intrinsic spatial resolution of a light sharing PET detector with 3 mm scintillation crystal. From the results, we can expect to achieve better system spatial resolution by identifying ICS events using convex optimization method and recovering them into the first interaction position.

Bibliography

1) Phelps, M. E. (2000). Positron emission tomography provides molecular imaging of biological processes. *Proc Natl Acad Sci U S A, 97*(16), 9226-9233.
2) Wienhard, K., Dahlbom, M., Eriksson, L., Michel, C., Bruckbauer, T., Pietrzyk, U., et al. (1994). The ECAT EXACT HR: performance of a new high resolution positron scanner. *J Comput Assist Tomogr, 18*(1), 110-118.
3) Chatziioannou, A. F., Cherry, S. R., Shao, Y., Silverman, R. W., Meadors, K., Farquhar, T. H., et al. (1999). Performance evaluation of microPET: a high-resolution lutetium oxyorthosilicate PET scanner for animal imaging. *J Nucl Med, 40*(7), 1164-1175.
4) Moses, W. W. (2011). Fundamental Limits of Spatial Resolution in PET. *Nucl Instrum Methods Phys Res A, 648 Supplement 1*, S236-S240. doi:10.1016/j.nima.2010.11.092
5) Cherry, S. R., Shao, Y., Silverman, R., Meadors, K., Siegel, S., Chatziioannou, A., et al. (1997). MicroPET: a high resolution PET scanner for imaging small animals. *IEEE Transactions on Nuclear Science, 44*(3), 1161-1166.
6) Cherry, S. R., Sorenson, J., & Phelps, M. E. (2012). Physics in nuclear medicine. 4th Edition. *Elsevier Health Sciences*.
7) Bailey, D. L., Townsend, D. W., Valk, P. E., & Maisey, M. N. (2005). *Positron emission tomography*: Springer.
8) MacDonald, L. R., & Dahlbom, M. (1998). Parallax correction in PET using depth of interaction information. *IEEE Transactions on Nuclear Science, 45*(4), 2232-2237.
9) Moses, W., & Derenzo, S. (1994). Design studies for a PET detector module using a PIN photodiode to measure depth of interaction. *IEEE Transactions on Nuclear Science, 41*(4), 1441-1445.
10) Lee, M. S., & Lee, J. S. (2015). Depth-of-interaction measurement in a single-layer crystal array with a single-ended readout using digital silicon photomultiplier. *Phys Med Biol, 60*(16), 6495-6514. doi:10.1088/0031-9155/60/16/6495
11) Lee, M. S., Kim, K. Y., Ko, G. B., & Lee, J. S. (2017). Prototype pre-clinical PET scanner with depth-of-interaction measurements using single-layer crystal array and single-ended readout. *Phys Med Biol, 62*(10), 3983-3996. doi:10.1088/1361-6560/aa64c7

12) Yang, Y., Wu, Y., Qi, J., St James, S., Du, H., Dokhale, P. A., et al. (2008). A prototype PET scanner with DOI-encoding detectors. *J Nucl Med, 49*(7), 1132-1140. doi:10.2967/jnumed.107.049791
13) Inadama, N., Murayama, H., Yamaya, T., Kitamura, K., Yamashita, T., Kawai, H., et al. (2006). Preliminary evaluation of four-layer BGO DOI-detector for PET. *IEEE Transactions on Nuclear Science, 53*(1), 30-34.
14) Saoudi, A., Pepin, C., Dion, F., Bentourkia, M., Lecomte, R., Andreaco, M., et al. (1999). Investigation of depth-of-interaction by pulse shape discrimination in multicrystal detectors read out by avalanche photodiodes. *IEEE Transactions on Nuclear Science, 46*(3), 462-467.
15) Ito, M., Lee, J. S., Kwon, S. I., Lee, G. S., Hong, B., Lee, K. S., et al. (2010). A four-layer DOI detector with a relative offset for use in an animal PET system. *IEEE Transactions on Nuclear Science, 57*(3), 976-981.
16) Yamaya, T., Mitsuhashi, T., Matsumoto, T., Inadama, N., Nishikido, F., Yoshida, E., et al. (2011). A SiPM-based isotropic-3D PET detector X'tal cube with a three-dimensional array of 1 mm3 crystals. *Physics in Medicine and Biology, 56*(21), 6793.
17) Yang, Y., Dokhale, P. A., Silverman, R. W., Shah, K. S., McClish, M. A., Farrell, R., et al. (2006). Depth of interaction resolution measurements for a high resolution PET detector using position sensitive avalanche photodiodes. Physics in Medicine and Biology, 51(9), 2131.
18) Ito, M., Lee, J. S., Park, M. J., Sim, K. S., & Hong, S. J. (2010). Design and simulation of a novel method for determining depth-of-interaction in a PET scintillation crystal array using a single-ended readout by a multi-anode PMT. *Phys Med Biol, 55*(13), 3827-3841. doi:10.1088/0031-9155/55/13/017
19) Joung, J., Miyaoka, R. S., & Lewellen, T. K. (2002). cMiCE: a high resolution animal PET using continuous LSO with a statistics based positioning scheme. *Nuclear Instruments and Methods in Physics Research Section A: Accelerators, Spectrometers, Detectors and Associated Equipment, 489*(1), 584-598.
20) Son, J.-W., Lee, M. S., & Lee, J. S. (2016). A depth-of-interaction PET detector using a stair-shaped reflector arrangement and a single-ended scintillation light readout. *Physics in Medicine and Biology, 62*(2), 465.
21) van Dam, H. T., Seifert, S., Vinke, R., Dendooven, P., Lohner, H., Beekman, F. J., et al. (2011). A practical method for depth of interaction determination in monolithic scintillator PET detectors. *Phys Med Biol, 56*(13), 4135-4145. doi:10.1088/0031-9155/56/13/025

22) Ito, M., Hong, S. J., & Lee, J. S. (2011). Positron emission tomography (PET) detectors with depth-of-interaction (DOI) capability. *Biomedical Engineering Letters, 1*(2), 70-81.
23) Du, H., Yang, Y., Glodo, J., Wu, Y., Shah, K., & Cherry, S. R. (2009). Continuous depth-of-interaction encoding using phosphor-coated scintillators. *Physics in Medicine and Biology, 54*(6), 1757.
24) Ito, M., Lee, M. S., & Lee, J. S. (2013). Continuous depth-of-interaction measurement in a single-layer pixelated crystal array using a single-ended readout. *Phys Med Biol, 58*(5), 1269-1282. doi:10.1088/0031-9155/58/5/1269
25) Miyaoka, R. S., Li, X., Lockhart, C., & Lewellen, T. K. (2009). *New continuous miniature crystal element (cMiCE) detector geometries.* Paper presented at the Nuclear Science Symposium Conference Record (NSS/MIC), 2009 IEEE.
26) Ling, T., Lewellen, T. K., & Miyaoka, R. S. (2007). Depth of interaction decoding of a continuous crystal detector module. *Phys Med Biol, 52*(8), 2213-2228. doi:10.1088/0031-9155/52/8/012
27) Frach, T., Prescher, G., Degenhardt, C., de Gruyter, R., Schmitz, A., & Ballizany, R. (2009). *The digital silicon photomultiplier—Principle of operation and intrinsic detector performance.* Paper presented at the Nuclear Science Symposium Conference Record (NSS/MIC), 2009 IEEE.
28) Jan, S., Santin, G., Strul, D., Staelens, S., Assie, K., Autret, D., et al. (2004). GATE: a simulation toolkit for PET and SPECT. *Phys Med Biol, 49*(19), 4543-4561.
29) Van Dam, H. T., Seifert, S., Vinke, R., Dendooven, P., Lohner, H., Beekman, F. J., et al. (2010). A comprehensive model of the response of silicon photomultipliers. *IEEE Transactions on Nuclear Science, 57*(4), 2254-2266.
30) Marcinkowski, R., Espana, S., Thoen, H., & Vandenberghe, S. (2012). *Performance of digital silicon photomultipliers for time of flight PET scanners.* Paper presented at the Nuclear Science Symposium and Medical Imaging Conference (NSS/MIC), 2012 IEEE.
31) Association, N. (2008). NEMA Standards Publication NU 4-2008. *Performance Measurements of Small Animal Positron Emission Tomographs*.
32) Ko, G. B., Kim, K. Y., Yoon, H. S., Lee, M. S., Son, J. W., Im, H. J., et al. (2016). Evaluation of a silicon photomultiplier PET insert for simultaneous PET and MR imaging. *Med Phys, 43*(1), 72. doi:10.1118/1.4937784

33) Shao, Y., Cherry, S. R., Siegel, S., & Silverman, R. W. (1996). A study of inter-crystal scatter in small scintillator arrays designed for high resolution PET imaging. *IEEE Transactions on Nuclear Science, 43*(3), 1938-1944.
34) Levin, C. S., & Zaidi, H. (2007). Current trends in preclinical PET system design. *PET clinics, 2*(2), 125-160.
35) Rafecas, M., Boning, G., Pichler, B. J., Lorenz, E., Schwaiger, M., & Ziegler, S. I. (2003). Inter-crystal scatter in a dual layer, high resolution LSO-APD positron emission tomograph. *Phys Med Biol, 48*(7), 821-848.
36) Alessio, A. M., Kinahan, P. E., & Lewellen, T. K. (2006). Modeling and incorporation of system response functions in 3-D whole body PET. *IEEE Trans Med Imaging, 25*(7), 828-837.
37) Panin, V. Y., Kehren, F., Michel, C., & Casey, M. (2006). Fully 3-D PET reconstruction with system matrix derived from point source measurements. *IEEE Trans Med Imaging, 25*(7), 907-921.
38) Grant, M., Boyd, S., & Ye, Y. (2008). CVX: Matlab software for disciplined convex programming. In.
39) Levin, A., & Moisan, C. (1996). *A more physical approach to model the surface treatment of scintillation counters and its implementation into DETECT.* Paper presented at the Nuclear Science Symposium, 1996. Conference Record., 1996 IEEE.
40) Comanor, K., Virador, P., & Moses, W. (1996). Algorithms to identify detector Compton scatter in PET modules. *IEEE Transactions on Nuclear Science, 43*(4), 2213-2218.
41) Lage, E., Parot, V., Moore, S. C., Sitek, A., Udias, J. M., Dave, S. R., et al. (2015). Recovery and normalization of triple coincidences in PET. *Med Phys, 42*(3), 1398-1410. doi:10.1118/1.4908226

Abstract in Korean

양전자단층촬영 (PET) 기법은 널리 사용되는 진단 영상 기법 중 하나로 분자 수준에서 생화학적 및 기능적 정보를 제공한다는 특성을 지니고 있다. PET 에서 획득한 분자 및 세포 수준의 진단 정보는 임상 및 전임상 수준에서 유용한 정보로서 사용되며, 이에 기반하여 새로운 질병의 진단 및 규명이 가능하다. 그러나 PET의 근본적인 특성 때문에 비롯되는 PET 영상의 좋지 않은 공간 해상도는 작은 크기의 병변을 진단하는 데에 있어 한계가 있다. 그러므로 PET의 진단 능력 극대화를 위하여 PET 장비의 공간 해상도 향상은 매우 중요하다.

이에 따라 본 연구에서는 고 해상도 PET 장비 개발을 위하여 PET 검출기의 3차원 위치 정보 정확도를 향상시키는 기술들을 개발하였다. 검출기의 3차원 위치 정보 정확도 향상을 위하여 PET 검출기 내에서 발생한 상호작용 반응깊이 (DOI) 정보와 섬광결정 간 산란현상 (ICS) 정보 추출 기술들을 개발하고 그 성능을 평가하였다. 그 첫 번째 연구내용으로서, 본 연구에서는 저 비용으로 개발 가능한 독창적 DOI 검출기를 개발하였고 그 성능을 평가하였다. 더 높은 DOI 위치 정보 정확도를 획득하기 위하여, 최대우도추정기법에 기반한 새로운 DOI 위치 정보 추출기법을 적용하였고 다양한 관점에서 검출기 최적화 연구를 진행하였다. 두 번째 연구내용으로서, 앞서 개발된 DOI 측정 및

추출 기술에 기반하여 원리 검증 용 DOI PET 시스템이 개발되었다. 개발된 DOI PET 시스템을 이용하여 검출기 및 시스템 성능이 평가되었고, DOI 기술이 실제 영상 해상도 향상에 어느 정도로 영향력이 있는지 평가하기 위하여 팬텀 및 동물 촬영이 진행되었다. 그 결과 본 연구에서 개발된 DOI 측정 및 추출 기술은 고 해상도 PET 시스템 개발에 매우 성공적으로 적용됨을 확인하였다. PET 검출기의 3차원 위치 정보 정확도 향상을 위하여 그 마지막 연구로서, 검출기 내에서 일어난 ICS 정보를 추출하는 새로운 기술을 개발하였다. 본 연구에서 개발한 기술은 기존의 기술로는 불가능하였던 빛 퍼짐 기반의 PET 검출기에서 ICS 정보 추출을 가능케 하였으며, 그 성능은 시뮬레이션 및 실험을 통하여 검증되었다. 본 연구에서 개발된 기술들을 통하여 최종적으로 3차원 위치 정보 정확도 향상을 통하여 PET 의 공간 해상도 향상이 가능함을 확인하였다.

Keyword : 양전자방출단층촬영 (PET), PET 검출기, 고해상도, 상호작용 반응깊이, 섬광결정 간 산란
Student Number : 2012-21778